Dedicated to Rev. Dr. Antony. T. Payyappilly

Heat transfer and flow characteristics study of an air-side radiator duct for different geometries

by

Geo Joy

ABSTRACT

In the heat exchanger of a power transformer, oil is cooled by the atmospheric air which flows around the radiator plate either due to buoyancy effects or using any forced means. This investigation is concentrated on the flow of air due to buoyancy effects. The scope of this thesis work is to investigate the heat transfer by buoyancy driven natural convection flow in the air side radiator ducts of a transformer. The investigation is limited to vertical ducts for smooth planar, smooth folded and rib-roughened geometries subjected to uniform heat flux. The study covers Rayleigh numbers ranging from 10^1 to 10^6 and focuses on the effect of channel geometry on the characteristic of flow and heat transfer as well as on the average and local Nusselt numbers. In this investigation, the effect of heat transfer with smooth planar geometry is studied and is compared with the other complex geometries. Certain parameters on the V-rib geometry are modified and its effect on heat transfer is also discussed.

All the models are designed with Gambit and the computations are done with FLUENT.

ACKNOWLEDGEMENTS

This work was conducted at ABB corporate Research, Vasteras, Sweden.

I would like to express my sincere gratitude to Dr. Carl-Olof Olsson, ABB Corporate Research for all his support, guidance and motivation. His encouragement has been a source of inspiration throughout the progress of this work.

I would like to convey my deepest regards to Prof. Håkan Nilsson for his valuable suggestions and guidance in writing the report. His short visits to ABB were very helpful for the progress of the project work.

I would like to thank Bertil Samuelsson, ABB Corporate Research for sharing his invaluable experience on CFD packages to me.

Finally, I would like to thank my colleagues at the ABB corporate Research who all created a pleasant working environment that enabled us to work efficiently.

NOMENCLATURE

c	constant in Rohsenow's correlation, Equation (23)
g	gravitational acceleration, m/s^2
H	height of the geometry, m
h	convection heat transfer coefficient
k	thermal conductivity, W/mK
P	pitch of V-ribs in multiple V-shaped rib geometry, m
p	pressure, Pa
R	radius, m
r	radius of the three arcs forming rib (rib height), m
S	wall distance, m
T	temperature, K
t	time, s
U	average velocity, m/s
u, v, w	velocity along x, y, and z coordinates, m/s
V	velocity, m/s
W	width of the geometry, m
X, Y, Z	x, y and z coordinates

A_c	area of a cross section, m^2
C_p	specific heat, J/KgK
D_h	hydraulic diameter, m
H_l	see Eq. (22)
q''	heat flux, W/m^2
T_b	bulk temperature, K
$T_{ij}^{(v)}$	viscous or deviatoric stresses
T_{in}	inlet temperature, K
T_o	initial temperature, K
T_w	wall temperature, K
T_{wavg}	average wall temperature, K
U_m	bulk velocity of the cross section, m/s

Greek Symbols

β	coefficient of thermal expansion of air, 1/K
μ	dynamic viscosity, Kg/ms
υ	kinematic viscosity, m^2/s
θ	angle of attack of ribs to the flow in multiple V shaped rib geometry
ρ	density, Kg/m^3
ρ_o	initial density, Kg/m^3
α_f	thermal diffusivity, m^2/s

Non-dimensional quantities

Gr	Grashof number
Nu	Nusselt number
Pr	Prandtl number
Re	Reynolds number
Ra	Rayleigh number

Nu_{avg}	average Nusselt number
$Nu_{S,avg}$	Nusselt number with average wall temperature
Nu_{fd}	Nusselt number at fully developed duct flow
Nu_{plate}	Nusselt number for vertical plate
Nu(y)	local Nusselt number

Subscript

avg	average
b	bulk
in	inlet
i, j, k	cartesian indexes
wavg	wall average
w	wall

CONTENTS

1 INTRODUCTION

Considerable attention has been given to buoyancy induced flow in vertical channels due to its application in cooling of electronic equipment. This study is motivated mainly by its application in the cooling of the radiator in a power transformer.

In a transformer, the core and windings are bathed in oil and the oil is circulated throughout the transformer. This is done for the cooling of the hot transformer elements. The oil gets heated up after some time, which brings up the necessity of a heat exchanger to cool the oil. It is very important to cool the oil in order to avoid break-down of the transformer. In many transformers a series of long vertical plates, with atmospheric air flowing in the adjacent channels to the heated oil, is used as heat exchangers. These are called radiators. These radiators extract heat from the oil to the atmospheric air. The rate at which heat is transferred from the plates of a radiator to the atmospheric air depends on certain parameters like distance between the plates, length of the plates, means of motion of air between the plates etc. Shape of the plates in the radiator also has a large effect on its efficiency in extracting heat from the oil to air. In this investigation, heat transfer on the air side of the radiator plates for different geometries is investigated and compared.

Natural convection is an energy transport process which takes place as a result of buoyancy-induced fluid motion occurring in the presence of a body force field. Buoyancy induced cooling is commonly used in the radiators of the power transformers. In fact, it is of great interest to design radiators compatible with both the forced and natural convective flows for a power transformer. The radiator plates designed for the cooling in a power transformer by means of natural convection are often very long. The length of the radiator plates plays a significant role to increase the velocity of the flow. This in turn increases the heat transfer in buoyancy-driven flows, while for the forced convection the velocity of the flow could be controlled by external means. It is appealing to optimize the size of the radiators without affecting the rate of heat transfer.

Three geometries are considered in this investigation for the study of heat transfer in the radiator of a transformer

1. Smooth Planar
2. Smooth Folded
3. Multiple V- shaped Rib Geometry

All the three geometries can be used as radiator plates for a transformer.

The heated parallel-walled channel is the quintessential configuration where the heat transfer characteristics of the buoyancy-induced flow are studied. Extensive researches have been undergone in the flow inside smooth heated channels so far to understand the mechanisms involved and to provide more information necessary for the optimization of the design for the heat transfer. The first comprehensive study of the parallel channel was reported by Elenbaas (1942). He established overall heat transfer correlations for isothermal channels over a wide range of thermal and geometric parameters. Later on, many researches have helped to improve our understanding of the mechanisms involved in the heat transfer between the parallel walls. Researches by Bodoia and Osterle (1962), Kettleborough (1972), Nakamura et al. (1982), and Bar-Cohen and Roshenow (1984) provide useful information in the study of heat transfer between the parallel plates. There are numerous investigations reported in which the downstream region is also included along with the parallel walls. Investigations by Chang and Lin (1989), Ramanathan and Kumar (1991), Shyy et al. (1992), and Morrone et al. (1997) are some of the examples. These investigations show the importance of the downstream region in the calculation of the flow rate though the Nusselt number remains unaffected.

For practical reasons, radiator plates are often corrugated or folded. These folds on the parallel plates would increase the area of interaction of air with the heated wall. The effect of the folds on the heat transfer characteristics is also studied.

Ribs on the plate might induce a secondary flow which in turn mixes the flow well and enhances the heat transfer in a duct. The concept of multiple V-shaped ribs are described in Olsson & Sunden (1997a) and Olsson & Sunden (1997b) where the performance of multiple V-shaped ribs was compared to the performance of a number of other rib-roughness geometries. It was found that multiple V-shaped ribs provided higher heat transfer than the parallel and crossed ribs, the difference being more pronounced at Reynolds numbers below 2000. The rib angle of the multiple V-rib geometry is taken as $45°$ which optimizes the heat transfer rate according to Olsson & Sunden (1998). The effect of ribs on the Nusselt number and the Reynolds number is also investigated by Olsson & Sunden (1998).

1.1 Smooth Planar

Figure 1 and 2 shows the two and the three-dimensional geometries of the smooth planar case which have been used for the present investigation. In this case, two smooth vertical walls are heated and the effect of air flow due to the buoyancy effects in-between the heated walls are investigated. The gradients along the Z-direction could be assumed as zero which simplifies the flow in-between the two vertical walls and yields the two dimensional case. This model can be used to understand the flow behavior and heat transfer characteristics for this kind of flow. The smooth planar case is investigated and compared with available correlations. Results from this particular case are used for validating the results of other two complex geometries.

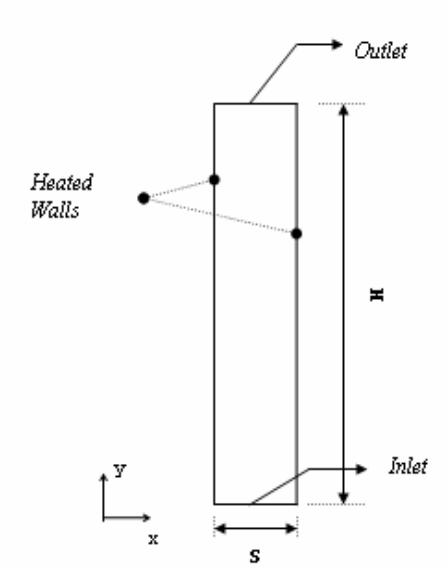

Figure 1: Two-dimensional Smooth planar

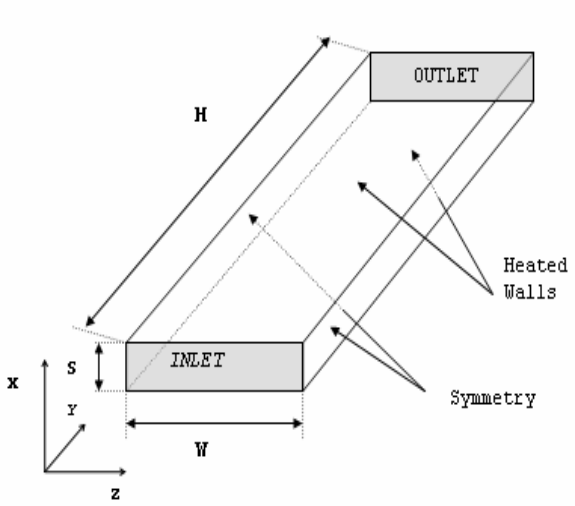

Figure 2: Three-dimensional Smooth planar

.

1.2. Smooth Folded

The smooth folded geometry increases the area of the plate that is exposed to the air and increases the mixing in the flow which can have a positive effect on the heat transfer. Since heat exchangers are quite large devices, it is quite important to come up with different geometries which can decrease the size of the heat exchangers without affecting the heat transfer efficiency. For the present investigation, the smooth folded geometry shown in figure 3 and figure 4 is studied and compared with the other two geometries.

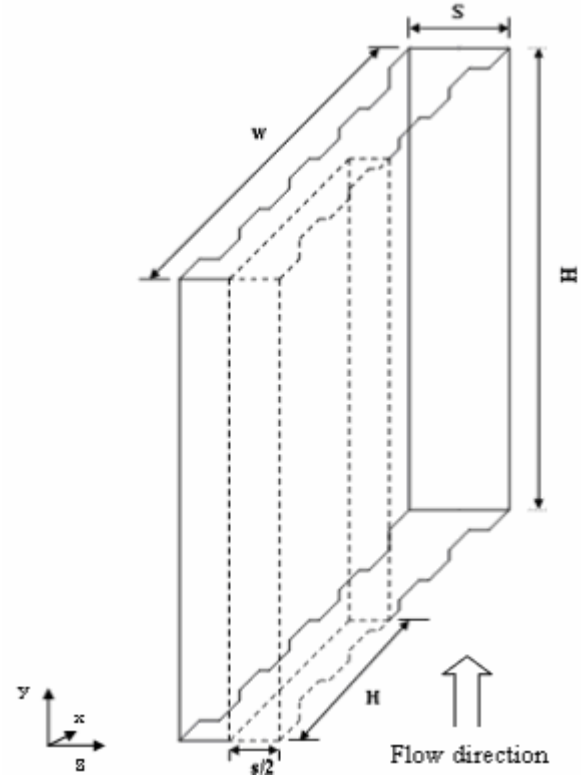

Figure 3: Three-dimensional Smooth-folded

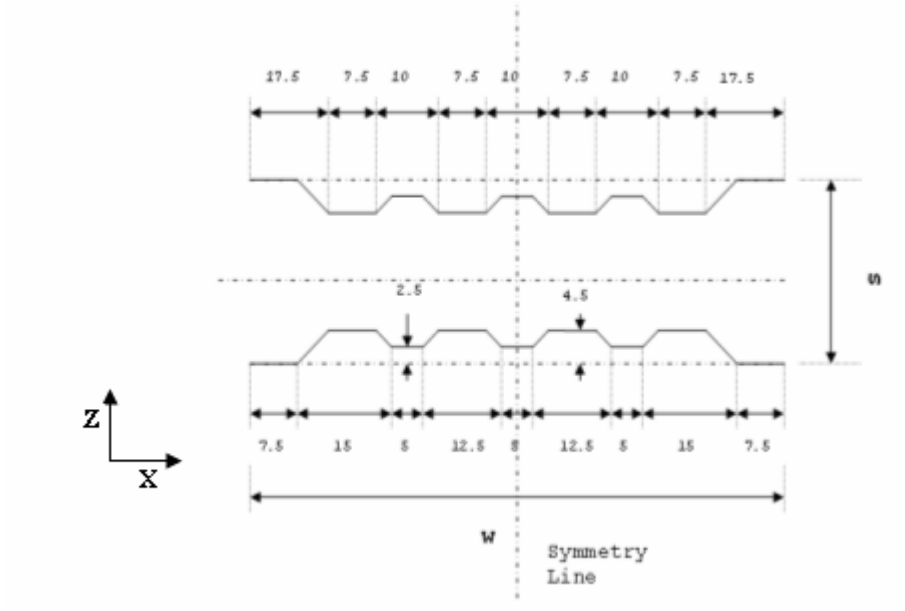

Figure 4: Top view of Smooth-folded

1.3 Multiple V shaped rib Geometry

Figure 5 shows a part of the multiple V-rib geometry together with the geometrical parameters that are considered for this investigation. The pitch considered for this investigation is 20 mm and 40 mm while the rib angle is taken as $\theta = 45°$. The V-ribs on the one wall is pointing downstream while on the other they are pointing upstream. Figure 6 shows the cross section of the ribs which is defined by three arcs with the same radii. The grey area shown in figure 5 indicates the computational domain. The computational domain is explained in detail in the section 3.2.3. The influence of the rib on the heat transfer and flow characteristics is studied and compared with the smooth planar case. The effect on the heat transfer with an increase in height, pitch and rib length is also evaluated.

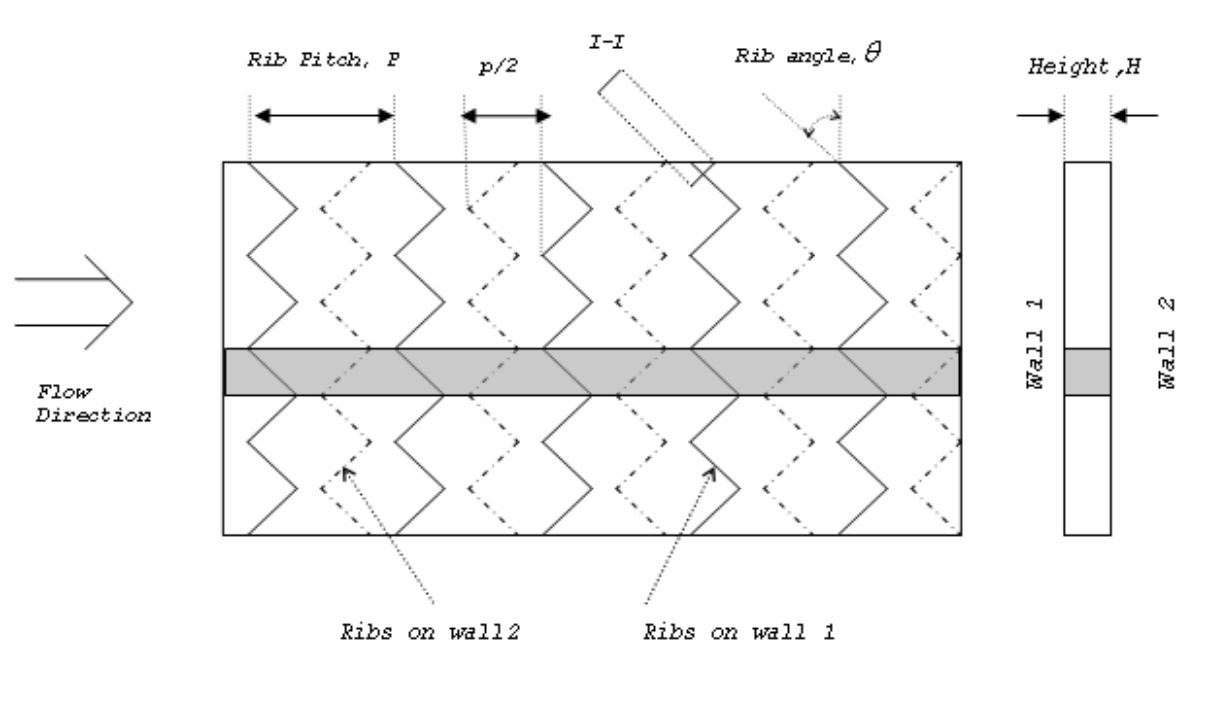

Figure 5: V-rib geometry

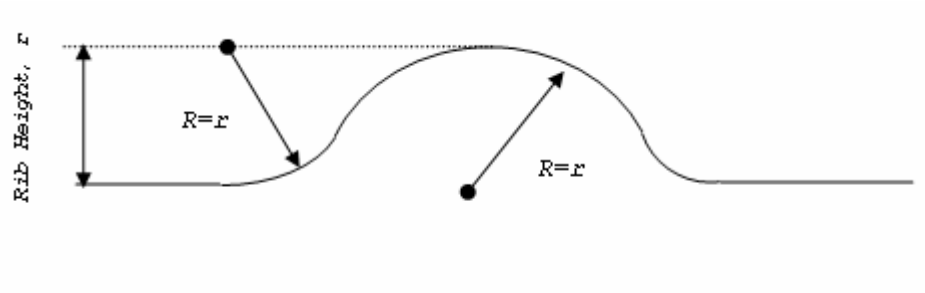

Figure 6: Cross section I-I of Figure 5

2 GOVERNING EQUATIONS

The governing equations are derived from the basic laws of conservation of mass, momentum and energy. The continuity equation is

$$\left\{\frac{\partial \tilde{\rho}}{\partial t}+u_j\frac{\partial \tilde{\rho}}{\partial x_j}\right\}+\tilde{\rho}\frac{\partial \tilde{u}_j}{\partial x_j}=0 \qquad (1)$$

Assuming the flow to be incompressible implies that the derivative of density of the fluid is zero, the above continuity equation can be written as

$$\frac{\partial u_i}{\partial x_i}=0 \qquad (2)$$

The assumptions made in this particular investigation are that the flow is laminar, incompressible, steady and with no viscous dissipation of thermal energy.

$$\rho\left[\tilde{u}_j\frac{\partial \tilde{u}_i}{\partial x_j}\right]=-\frac{\partial \tilde{p}}{\partial x_i}+\frac{\partial \tilde{T}_{ij}^{(v)}}{\partial x_j}-\frac{g_i}{\rho}(\rho-\rho_o) \qquad (3)$$

For incompressible flows, $\tilde{\rho}=\rho$ and viscosity is constant throughout the flow, the instantaneous momentum equation (3) reduces to

$$\tilde{u}_j\frac{\partial \tilde{u}_i}{\partial x_j}=-\frac{1}{\rho}\frac{\partial \tilde{p}}{\partial x_i}+\nu\frac{\partial^2 \tilde{u}_i}{\partial x_j\partial x_j}-\frac{g_i}{\rho}(\rho-\rho_o) \qquad (4)$$

But in this flow with natural convection, the gravity is aligned with the Y-direction and hence the gravity term only occurs in the v-momentum equation, yielding

$$u\frac{\partial v}{\partial x}+v\frac{\partial v}{\partial y}+w\frac{\partial v}{\partial z}=-\frac{1}{\rho}\frac{\partial p}{\partial y}+\nu\left(\frac{\partial^2 v}{\partial x^2}+\frac{\partial^2 v}{\partial y^2}+\frac{\partial^2 v}{\partial z^2}\right)-\frac{g}{\rho}(\rho-\rho_o) \qquad (5)$$

The Boussinesq approximation is used in the equation (5). This approximation is commonly understood to consist of the following.

1. Density is assumed as constant except when it directly causes buoyant forces. This means that the continuity equation has its incompressible form and that density is considered variable only in the gravitational term of the momentum equation.

2. All other fluid properties are assumed constant

3. Viscous dissipation is assumed to be negligible

These last two points simplify the equations so that attention is focused on the effect of buoyancy. The validity of boussinesq approximation could be referred in Donald & Aldo (1975).

So, as a result of this application we can say that density variations are due only to temperature variations and hence $(\rho - \rho_o)$ may be related to a fluid property known as the volumetric thermal expansion coefficient.

$$\beta = -\frac{1}{\rho}\left(\frac{\partial \rho}{\partial T}\right)_p \qquad (6)$$

This can be approximated as $\beta \approx -\frac{1}{\rho}\frac{\Delta\rho}{\Delta T} = -\frac{1}{\rho}\frac{\rho - \rho_o}{T - T_o}$

and it becomes

$$\rho - \rho_o \approx -\rho\beta(T - T_o) \qquad (7)$$

Applying boussinesq

$$u\frac{\partial v}{\partial x} + v\frac{\partial v}{\partial y} + w\frac{\partial v}{\partial z} = -\frac{1}{\rho}\frac{\partial p}{\partial y} + \nu\left(\frac{\partial^2 v}{\partial x^2} + \frac{\partial^2 v}{\partial y^2} + \frac{\partial^2 v}{\partial z^2}\right) + \beta g(T - T_O) \qquad (8)$$

This is the Y-direction momentum equation where all fluid properties including density may be assumed constant for small density/temperature changes.

The heat transfer part of the convection problem requires a solution for the temperature distribution through the flow. The additional equation for accomplishing this ultimate objective is the first law of Thermodynamics or the energy equation which is the law of physics that states that heat absorbed by a system either raises the internal energy of the system or does work on the environment.

The energy equation for an incompressible, steady flow without viscous dissipation can be written as

$$u\frac{\partial T}{\partial x} + v\frac{\partial T}{\partial y} + w\frac{\partial T}{\partial z} = \frac{k}{\rho C_p}\left(\frac{\partial^2 T}{\partial x^2} + \frac{\partial^2 T}{\partial y^2} + \frac{\partial^2 T}{\partial z^2}\right) \qquad (9)$$

2.1 Non-dimensional numbers

In this section important non-dimensional numbers are explained.

2.1.1 Rayleigh number

The Rayleigh number (Ra) for a fluid is a non-dimensional number associated with the heat transfer within the fluid. The Rayleigh number can be defined as the ratio of the product of buoyancy forces and heat advection and the product of viscous forces and heat conduction of the fluid.

It is equal to the product of the Grashof and Prandtl numbers
$Ra = Gr\,\mathrm{Pr}$

The vertical parallel plates of these geometries can have either uniform wall temperature boundary condition or uniform heat flux boundary condition. The uniform heat flux boundary condition is considered throughout the investigation and the following expression for the Rayleigh number based on surface heat flux ($q^{"}$) is used.

$$Ra = \frac{g\beta q^{ll} S^4}{\alpha_f \upsilon k (H/S)} \qquad (10)$$

2.1.2 Prandtl number

The Prandtl Number is the ratio of the momentum diffusion to the heat diffusion. In this case, the fluid used is air, and the Prandtl number for air is 0.71

$$\mathrm{Pr} = \frac{\mu C_p}{k} = \frac{\upsilon}{\alpha_f} \qquad (11)$$

2.1.3 Reynolds number

The Reynolds number is the ratio of inertia force to viscous force.

$$\mathrm{Re} = \frac{UL}{\upsilon} \qquad (12)$$

In this case we consider the Reynolds number using the hydraulic diameter as length scale

i.e.

$$\mathrm{Re} = \frac{UD_h}{\upsilon} \qquad (13)$$

For a rectangular duct $D_h = \dfrac{4A_c}{perimeter}$ or $\dfrac{4 \times Volume}{\text{Surface Area}}$

2.1.4 Nusselt number

The Nusselt number is the ratio of convective heat transfer to the heat transfer that would occur under the same conditions, but only due to pure conduction. Nusselt number depends on the rate of heat transfer from the plate to the fluid

$$Nu = \frac{hl}{k} \tag{14}$$

The length scale (l) is taken as the duct width S

The average Nusselt Number is given as

$$Nu_{avg} = \frac{q^{ll} S}{(T_{wavg} - T_{in})k} \qquad \text{Where } T_{wavg} = \frac{1}{H}\int_0^H T_w dy \tag{15}$$

The local Nusselt number is given as

$$Nu(y) = \frac{q^{ll} S}{(T_w(y) - T_b(y))k} \tag{16}$$

where $T_b(y)$ is the bulk temperature given by

$$T_b(y) = \frac{1}{SV}\int_0^S T(x)V(x)dx \tag{17}$$

where

$$V = \frac{1}{S}\int_0^S V(x)dx \tag{18}$$

In the equation (17) and (18)
V(x) is the velocity at each node along the X-direction.
T(x) is the temperature at each node along the X-direction.

2.2 Correlations

The following correlations are compared and analyzed by Olsson C.-O. (2004) for buoyancy induced flow between vertical parallel plates.

2.2.1 Ramanathan and Kumar

The following formula for the average Nusselt number is given by Ramanathan and Kumar (1991)

$$Nu_{S,avg} = \left[\frac{185}{(H/S)^5} + (23Ra^{-1.3} + 0.5Ra^{-0.6})^{-1.25} \right]^{0.2} \quad (19)$$

This correlation is valid for $1 \le \frac{H}{S} \le 15$, $10 \le Ra \le 3\times10^5$ and Pr = 0.7

The first term is in order to account for the increase in Nusselt number due to conduction effects that can be important for small Ra and small H/S.

2.2.2 Rohsenow

The expression recommended by Rohsenow et al. (1998) is

$$Nu_{s,avg} = \left[(Nu_{fd})^{-3.5} + (Nu_{plate})^{-3.5} \right]^{-(1/3.5)} \quad (20)$$

Where

$$Nu_{s,avg} = \frac{q''}{T_{avg} - T_{in}} \frac{S}{k_f} \quad (21)$$

$$Nu_{fd} = .29(Ra)^{1/2} \quad (22)$$

$$Nu_{plate} = cH_l(Ra)^{1/5} \quad (23)$$

$$H_l = \frac{6}{5}\left(\frac{\Pr}{4 + 9\sqrt{\Pr} + 10\Pr}\right)^{1/5} \quad (24)$$

3 NUMERICAL ASPECTS

This section deals with the numerical considerations. The set-up of boundary conditions and the grid design is discussed for all geometries.

The flow field is subdivided into finite volumes, each of which encloses a node. Scalar variables such as temperature are evaluated at the grid node, while to compute face pressure the discrete continuity balance for a "staggered" control volume about the face is used. The momentum and thermal fields are coupled in buoyancy driven flows. Hence they are solved together which in turn increase the tendency of being unstable.

The under-relaxation factors used are shown in Table 1 for the smooth planar, the smooth folded and the V-rib geometries.

Table 1 : Under-relaxation factors

Geometry	Momentum	Energy	Body Force	Pressure
Smooth planar	0.7	0.98	0.45	0.20
Smooth Folder	0.4	0 98	0.40	0.20
V-Rib	0.4	0.90	0.30	0.15

3.1 Solver

The solver that is used for all the three geometries is the segregated solver and the pressure and velocity are coupled. The pressure velocity coupling scheme which has been used for the investigation is SIMPLE.

The schemes used for solving the momentum and energy equations for the two-dimensional smooth planar geometry is the second-order upwind scheme and for all other geometries are first order upwind scheme. In this case the second-order upwind scheme makes the convergence very unstable. So the choice was first-order upwind for these cases and the pressure interpolation scheme which is used is PRESTO. Since the flow is aligned to the grid and is a laminar flow with quadrilateral and hexagonal grid all throughout, first-order upwind scheme gives a reasonably good accuracy though it is not as accurate as second-order upwind.

3.2 Computational Domain

In this section the cases are described in more detail.

3.2.1 Smooth Planar

Both the two-dimensional and the three-dimensional geometries are studied for the smooth planar case in this investigation. The computational domains of both the geometries are shown in Figure 7 and Figure 8. The extension at the inlet has the purpose of giving a suitable inlet boundary condition.

3.2.1.1 Boundary conditions

Figure 7 shows the domain that is used for the computational purpose along with the boundary conditions given. Since this case is a natural convection case, the definition of the inlet boundary condition can always be a problem. It is impossible to give velocity inlet boundary condition or mass flow inlet boundary condition since both of these are not known in this buoyancy induced flow. Hence the computational domain is extended further down so as to define the inlet boundary as a pressure inlet boundary condition. But the width and size of the extended portion should be designed so that it doesn't affect the flow at the inlet. In this investigation, an inlet box is extended to a length of 2S towards each side of the inlet, which is assumed as far away enough from the inlet. The two walls at the sides of the channel are given a uniform heat flux boundary condition (UWF) and the extended edges are given a wall boundary condition with zero heat flux.

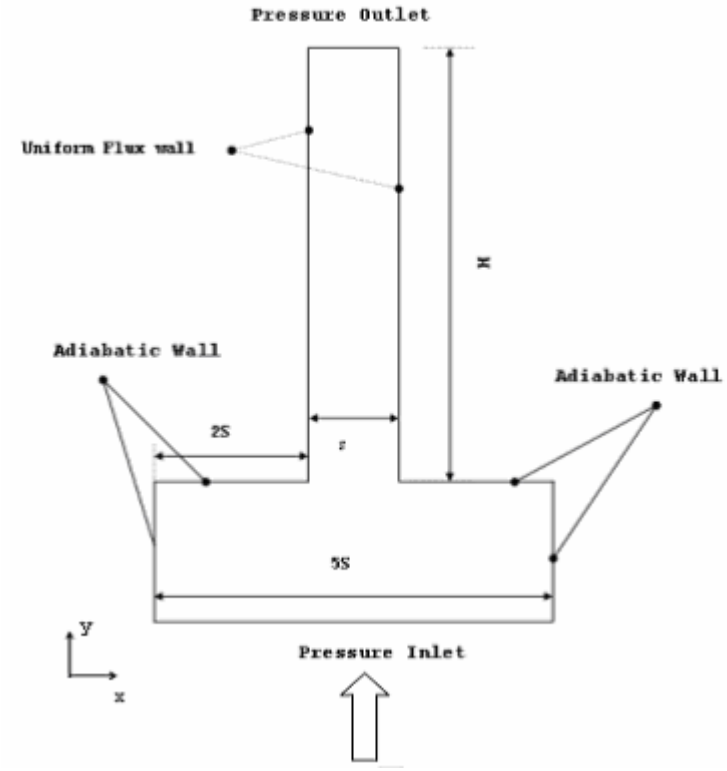

F igure 7: *Two-dimensional smooth planar domain*

Figure 8 shows the computational domain that is used for the three-dimensional smooth planar case, and table 2 shows the boundary conditions given. In the three-dimensional case, the flow is considered as homogeneous along the Z-direction (throughout the width (W)). The three dimensional case is done for the purpose of validating the model with the two dimensional results. The extension-inlet box is not extended in the Z-direction because it behaves symmetrical towards that direction. Symmetry boundary conditions are given along the planes HRKF and LECD that are not extended.

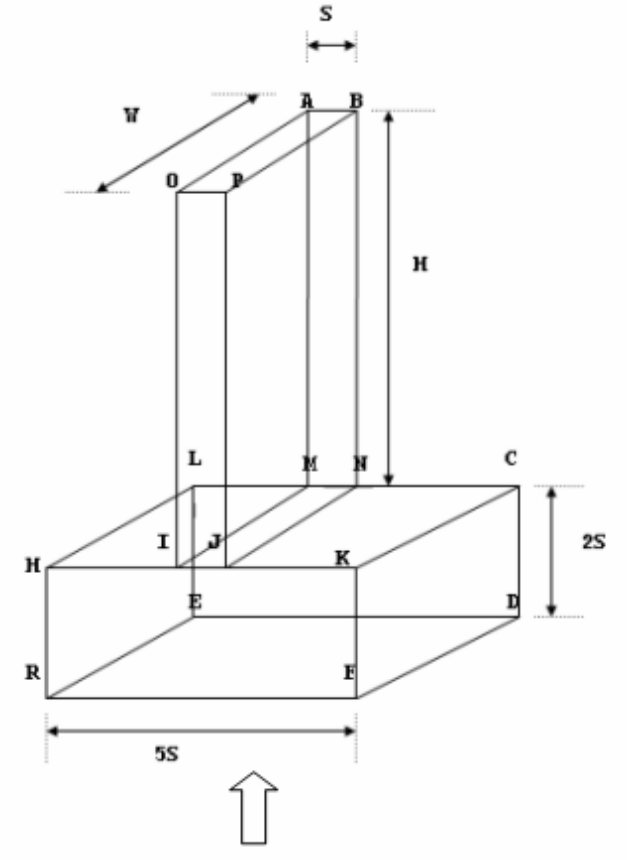

Table 2: Boundary conditions

Sl.No.	Face	Boundary Condition
1	ERFD	Pressure Inlet
2	ABOP	Pressure Outlet
3	PBJN	Wall
4	AOMI	Wall
5	JNCK	Wall
6	KCFD	Wall
7	MILH	Wall
8	LERH	Wall
9	HRKF	Symmetry
10	LECD	Symmetry
11	IJOP	Symmetry
12	ABMN	Symmetry

Figure 8: Three-dimensional smooth planar domain

The dimensions given for the smooth planar case are
S = 20 mm
H = 200 mm, 400 mm
W = 4S = 80 mm

3.2.1.2 Grids

Figure 9 shows the grid of the channel and the extended portion in a smooth planar channel. In the three dimensional case, the grid used is coarse in the Z-direction because the flow is considered to have no gradients along that direction. Normal to the heat flux wall regions, sharp gradients are expected and so a denser grid is used in that region.

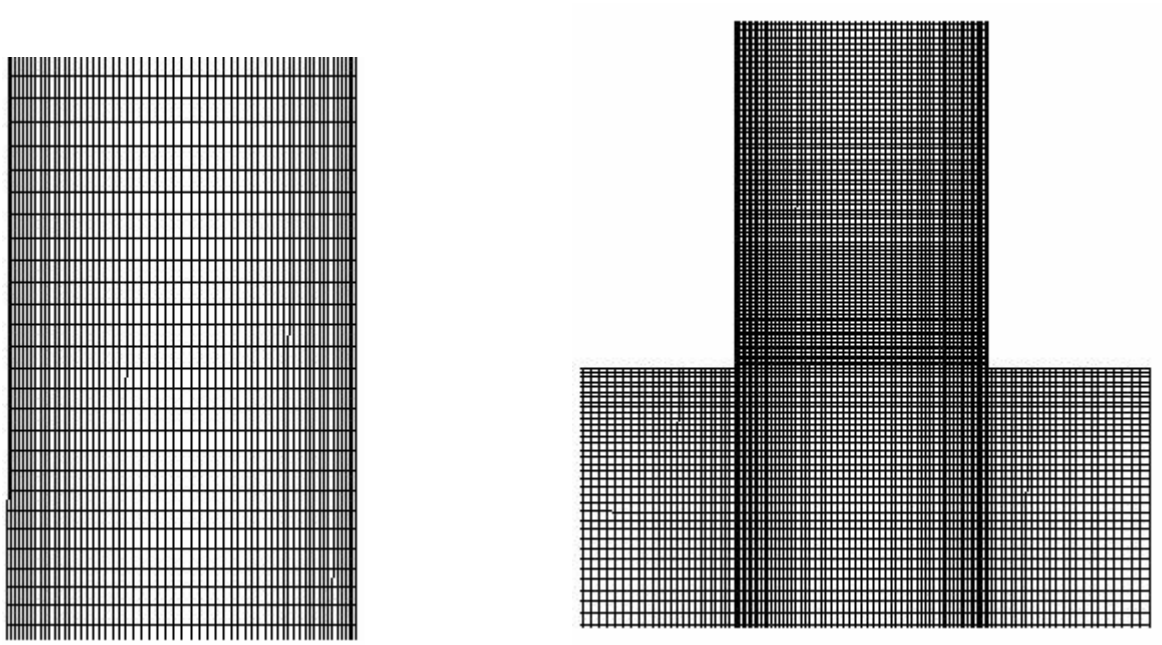

(a) Zooming of the channel *(b) Inlet extension*

Figure 9: Grid distribution for smooth planar

Different Grid configurations were tested and the present grid is selected as the one which provides satisfactory results at a reasonable computational cost. The grid sizes for the two and the three dimensional cases were 25000 and 200,000 respectively.

3.2.2 Smooth folded

The boundary conditions and the grid used for the smooth folder case are discussed in this section.

3.2.2.1 Boundary conditions

The smooth folded case which is shown in figure 3 is the real model which is to be investigated. For the computational purpose, only one quarter of the model is considered because all other parts of the smooth folded geometry may be as symmetrical to it. Figure 10 and Table 3 show the computational domain and the boundary conditions given for this particular case. As in the smooth planar case, the inlet is extended for the purpose of defining the inlet boundary condition.

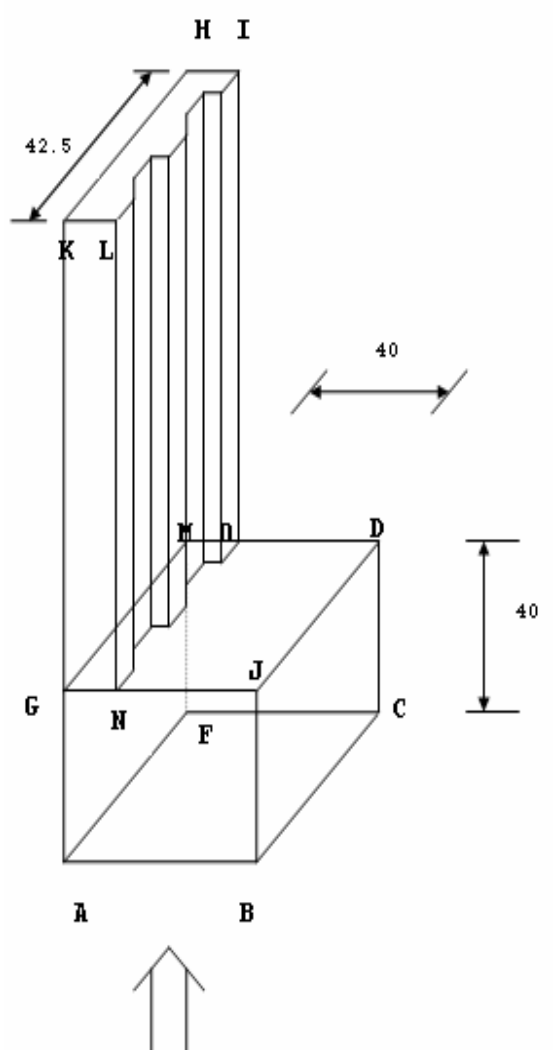

Figure 10: Computational domain for the smooth folded geometry

Table 3: Boundary conditions

Sl.No	Face	Boundary Condition
1	ABCF	Pressure Inlet
2	KLHI	Pressure Outlet
3	KHMG	Wall
4	NODJ	Wall
5	JDCB	Wall
6	ABGJ	Symmetry
7	GNKL	Symmetry
8	MOHI	Symmetry
9	MDCF	Symmetry
10	AFMG	Symmetry
11	GMHK	Symmetry

3.2.2.2 Grids

Figure 11 shows the outlet of the computational domain of the smooth folded case. The grid used in the dotted folded faces of the outlet 'a' and 'b' in figure 11 is shown in figure 12. In the folded geometry, the grid that is used in the folded region near the wall is quite important to get a good convergence and reasonably good results. Careful attention must be given to have a good resolution of the grid normal to the inclined walls of the folded areas. The grid cells used are small enough to capture the behavior of the sharp gradients near to the wall. Mesh dependence is checked with much coarser mesh. The number of grid for the smooth folded geometry is 310,000.

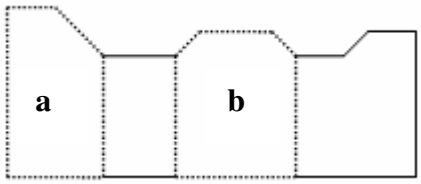

Figure 11: Outlet of the computational domain for smooth folded case

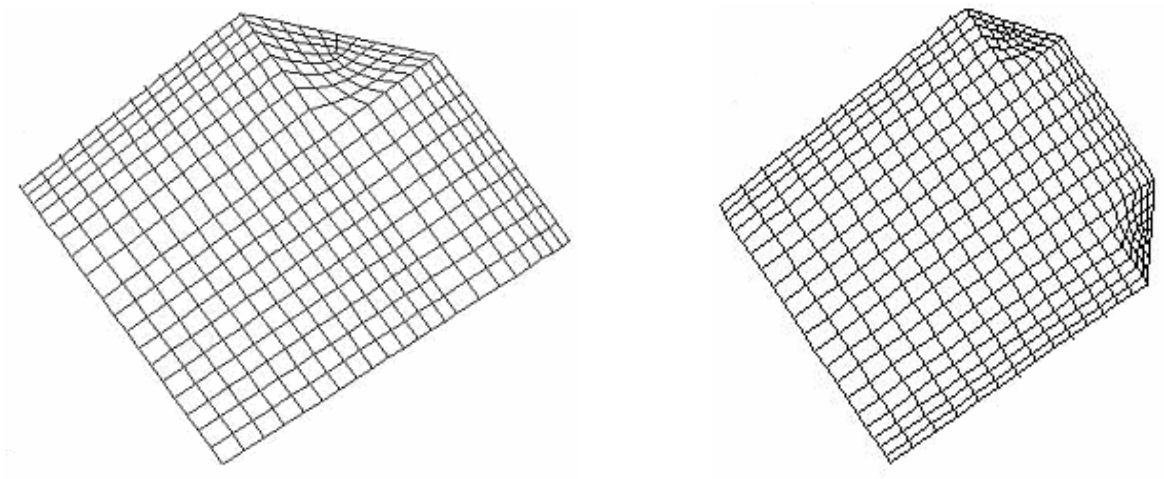

Figure 12: Grid distribution of the dotted folded faces 'a' and 'b' shown in figure 11

3.2.3 Multiple V shaped rib Geometry

The boundary conditions and the grid used for the V-rib geometry are discussed in this section.

3.2.3.1 Boundary conditions

Figure 13 shows the computational domain considered for the V-rib geometry for the present investigation. This computational domain is a part of the whole geometry that is the grey portion in figure 5 . The remaining area that is not considered for the computational study might be considered as symmetry boundary condition since it behaves in a symmetrical manner with respect to the area of study. The cross-view of the V-rib domain is shown in figure 14.

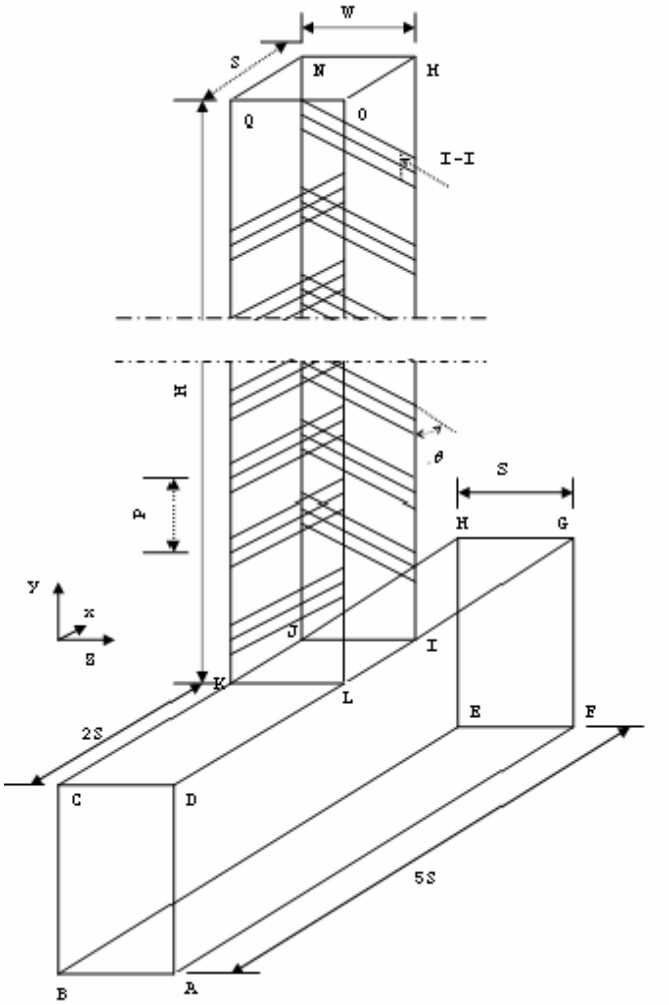

Figure 13: Computational domain for V-rib

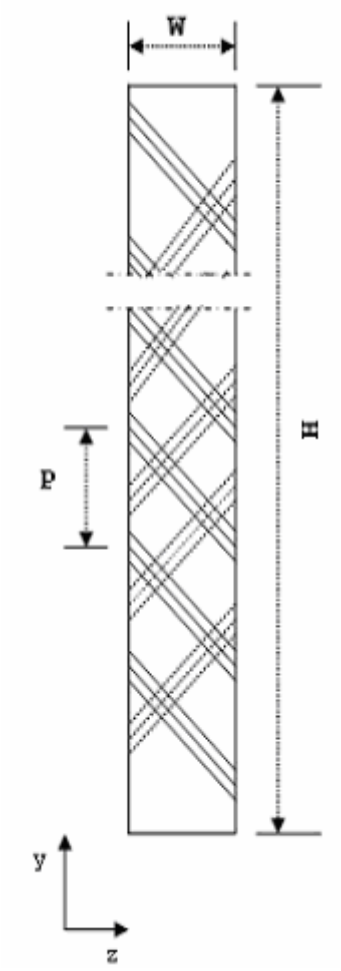

Figure 14: Cross-View of the V-rib domain

The cross section I-I in Figure 13 is shown in Figure 6. The smooth curve of the rib is set at an angle of attack to the flow.

Table 4: Boundary conditions for V-rib geometry

Sl.no	Faces	Boundary conditions
1	ABEF	Pressure Inlet
2	MNOQ	Pressure Outlet
3	KLOQ	Wall
4	MNIJ	Wall
5	GHIJ	Wall
6	EFGH	Wall
7	CDLK	Wall
8	ABCD	Wall
9	AFGD	Symmetry
10	EHBC	Symmetry
11	ILOM	Symmetry
12	KJNQ	Symmetry

Table 4 shows the boundary conditions defined for the V-rib geometry. Walls KLOQ and MNIJ are given different fluxes for each case corresponding to the Rayleigh numbers while all other walls are considered adiabatic. Defining the boundary conditions could always be the problem for the buoyancy-driven duct flows. A pressure inlet boundary condition is defined in an extended face (ABEF) from the Inlet (KLIJ).

3.2.3.2 Grids

The multiple V-shaped rib geometry is meshed with T-grid along with the hex core meshing scheme. This scheme creates a mesh consisting of two regions; the inner region composed of regular hexahedral elements and the outer region consisting of the pyramidal, tetrahedral and/or wedge elements as shown in figure 15. In the extension inlet box, structured hexahedral mesh is used which decreases the number of cells considerably. The grid distribution used for both the geometries is exactly the same for the comparisons to be accurate.

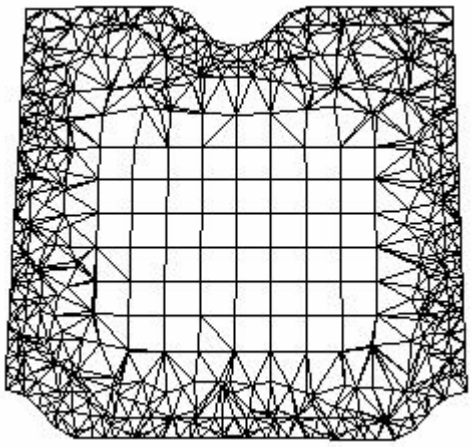

Figure 15: Grid distribution for Multiple V-shaped rib geometry

The number of grids for the multiple V-shaped rib geometry for 200 mm and 400 mm height are 300,000 and 500,000 respectively.

3.3 Cases Investigated

The smooth planar (two-dimensional and three-dimensional) and the V-rib geometries consider exactly the same parameters to investigate while for the smooth folded geometry it varies slightly, due to the complex nature of the smooth folded geometry along the Z-direction to assume a good value for 'S'.

Table 5: Cases investigated

Sl No	Heat Flux (W/m2)	Rayleigh Number		
		Smooth planar	Smooth folded	V-Rib
1	.13	10^1	8×10^1	10^1
2	1.3	10^2	8×10^2	10^2
3	13	10^3	8×10^3	10^3
4	130	10^4	8×10^4	10^4
5	1300	10^5	8×10^5	10^5
6	13000	10^6	8×10^6	10^6

Table 5 shows the cases investigated for all the geometries. Equation (10) is used to find the relation between the heat flux and the Rayleigh number. The smooth planar case is investigated for two different heights, for H= 200 mm and for H= 400 mm. The smooth folded geometry due to its folded shape, assuming a value for 'S' is puzzling because it has different values along the Z-direction. For this investigation, 'S' is taken as 30 mm for the smooth-folded case since it is the maximum value 'S' takes throughout the geometry. For all other geometries 'S' is 20 mm while for the smooth folded it is 30 mm which shows the reason for the difference in Rayleigh number considered for the smooth folded case.

The multiple V-rib geometry is investigated for different parameters. The pitch, the length of the channel and the height of the rib is doubled and its effect on the heat transfer characteristics is investigated.

The different parameters considered for all the geometries are shown in table 6

Table 6 : Parameters Investigated

Smooth Planar				
H (mm)	S (mm)	W (mm)		
200	20	80		
400	20	80		
Smooth Folded				
H (mm)	S (mm)	W (mm)		
200	30	85		
Multiple V-rib				
H (mm)	S (mm)	P (mm)	r (mm)	θ (Degree)
200	20	20	2	45
400	20	20	2	45
400	20	40	2	45
400	20	40	4	45

4 RESULTS AND DISCUSSIONS

The important flow parameters in this natural convection flow problem are the Rayleigh number (Ra) and the Prandtl number (Pr). The Rayleigh number varies from 10^1 to 10^6 in all the cases except for smooth folded case while the other parameters are maintained at a particular value (see table 5 and table 6 . The Prandtl number is 0.71 throughout the study since we are only interested in air flow. The heat transfer, the flow characteristics and the behavior of the non-dimensional numbers are discussed and compared with the available correlations for all the different geometries.

4.1 Smooth Planar

The flow behavior and the heat transfer characteristics of the smooth planar case are widely discussed in this section and the results are validated with the available correlations.

4.1.1 Inlet and outlet velocity profiles

Figure 16 shows the outlet velocity profile for the smooth planar case for different Ra. For low Ra, viscous effects are larger compared to the gravity effects and as a result due to the larger viscous diffusion, the presence of the heated wall is being influenced throughout the separation between the walls. But for the higher Ra, the gravity effects are much larger than the viscous diffusion, so the effects are mainly close to the walls. As the Ra increases, flattening of the velocity profile towards the centre of the channel increases and after a critical value of Ra, velocity decreases towards the centre of the channel. For Ra $=10^6$, the centre line velocity becomes close to zero. The trend of the velocity profile is that a further increase in Ra would decrease the centerline velocity to zero which concludes that the presence of heated wall is not sensed in the centre of the channel for higher Rayleigh numbers. It is obvious from figure 16 that as Ra increases; the velocity boundary layer becomes thinner.

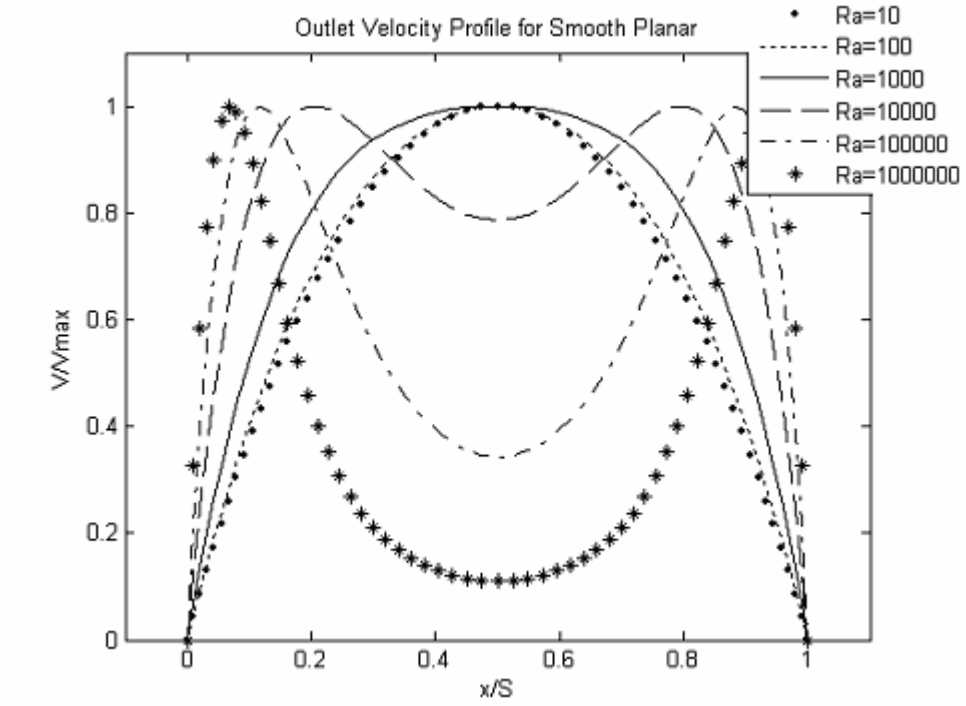

Figure 16: Outlet velocity profile for smooth planar

Figure 17 shows the inlet velocity profile of the smooth planar case. The inlet velocity profile shows that the trend in the development of the velocity profile is the same, right from the inlet for the smooth planar case.

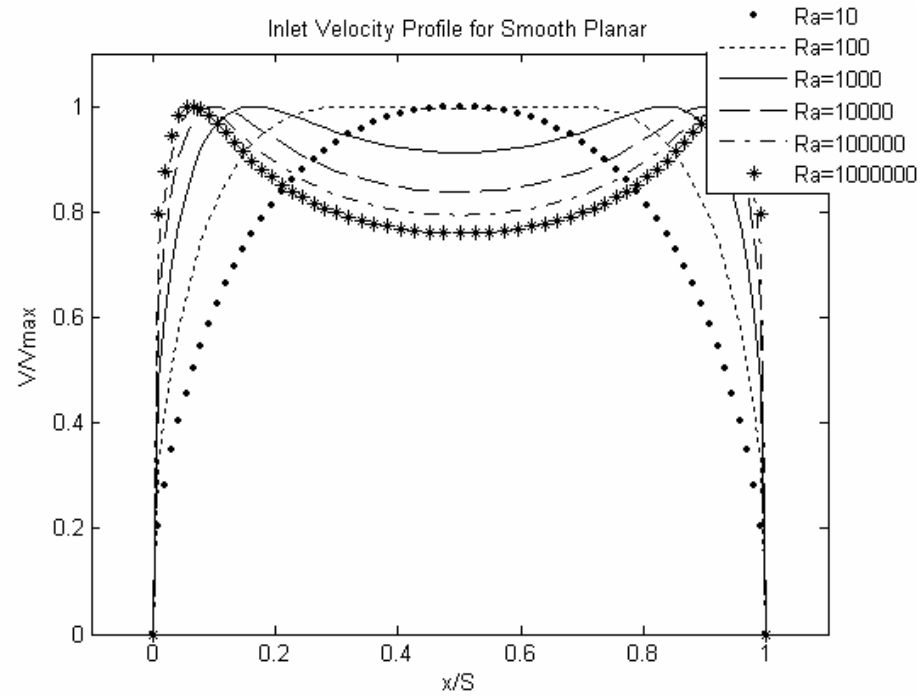

Figure 17: Inlet velocity profile for smooth planar

4.1.2 Outlet temperature profile

Figure 18, 19 shows the normalized outlet temperature profile for Ra 10^1 to10^6 . The outlet temperature profile of the smooth planar case tends to flatten as Ra increases. As the Rayleigh number increases the heat flux on the heated wall is also increased. Consequently the air close to the wall due to gravitational advection gets more heated in turn increasing the velocity of air-flow inside the channel. Eventually, it is obvious that for the highest Rayleigh numbers the region away from the heated walls remain unaffected by the temperature increase at the wall. This behavior of the temperature profile is similar to the velocity profile for higher Ra. The temperature boundary layer also becomes thinner as the Rayleigh number is increased. For Ra = 10^1 the temperature profile is seen as a straight line. This is because of the change in temperature for the lowest Rayleigh number is very less compared to the other Rayleigh numbers..

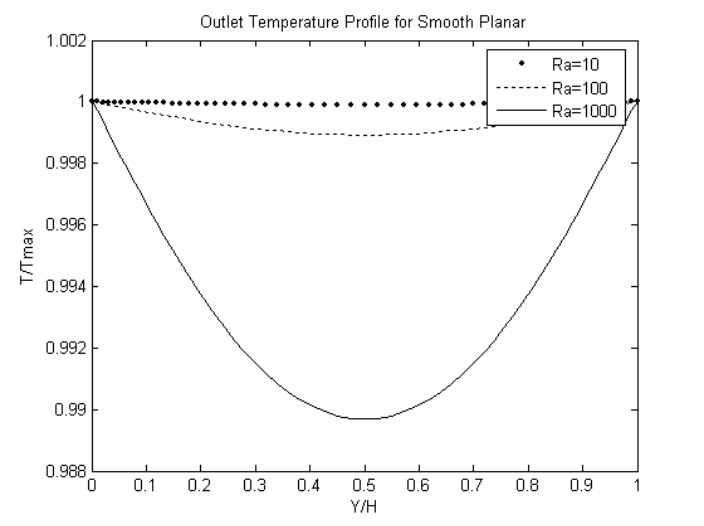

Figure 18: Outlet temperature profiles at Ra= $10^1, 10^2, 10^3$

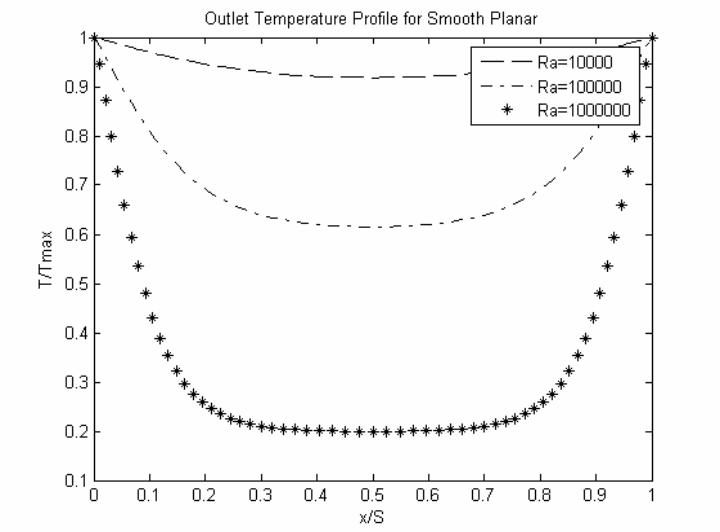

Figure 19: Outlet temperature profiles at Ra= 10^4, 10^5 *and* 10^6

4.1.3 Average Nusselt number versus Rayleigh number

In this section, the present data is validated against two correlations by Ramanathan and Kumar (1991) and Rohsenow et al. (1998) (see sections (2.2.1) and (2.2.2)). The values from the smooth planar case are further used to validate the results of the other two complex geometries.

Figure 20 shows that the results presented in this investigation give a good agreement with the correlation which is recommended by Ramanathan and Kumar (1991). At the investigated range of Rayleigh numbers, the present data under-predicts the value as compared to the correlation except for the highest Rayleigh number. For Ra=10^6 , the present data is in very good agreement with the Ramanathan and Kumar correlation. The correlation recommended by Ramanathan and Kumar (1991) is valid for $1 \le \frac{H}{S} \le 15$ and $10 \le Ra \le 3\times10^5$ for Pr = 0.7 and the vertical diffusion is assumed negligible in this correlation.

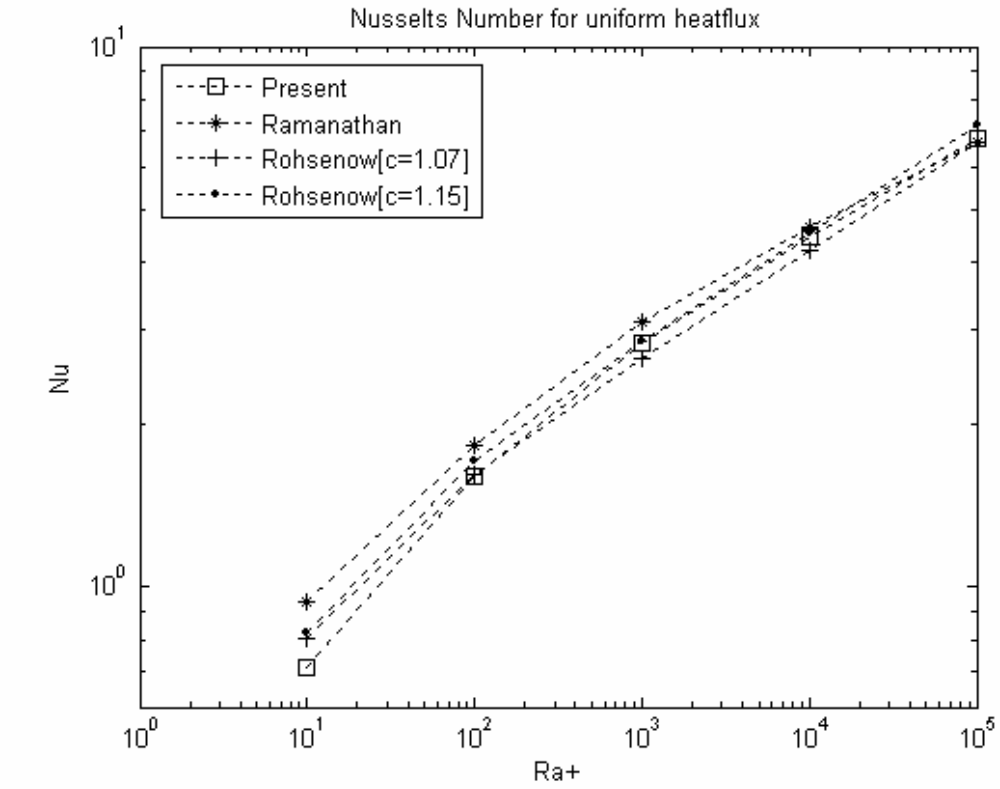

Figure 20: Average Nusselt number versus Rayleigh number

The present data is in good agreement with the correlation given by Rohsenow et al (1998). The present data shows a slight over-prediction for intermediate Ra but for low and high Ra it is in exact agreement with the Rohsenow's correlation when the c is given a value of 1.07. When the c is given a value of 1.15 it under-predicts slightly for the high and low Ra. But other than these slight deviations no matter whichever value c takes, the present data is in good agreement with the Rohsenow's correlation.

Accordingly the present data for smooth planar case is validated for further comparisons.

4.1.4 Local Nusselt number versus Y/H

Figure 21 shows the characteristics of the local Nusselt number for different Rayleigh numbers. It follows a general trend for all the Rayleigh numbers. Figure 22 (a) shows the local Nusselt number for Ra $=10^3$ along the Y-direction. It decreases as it goes towards the outlet, it shows a regular pattern similar to as for Ra $=10^4$ in figure 22 (b), except in the last three points. It might be the influence of the pressure outlet boundary condition. Ra $=10^3$ is more sensitive to the pressure outlet boundary condition as compared to Ra $=10^4$ because the variation of Nusselt number at Ra $=10^3$ is very small. For Ra $=10^5$, local Nusselt number in the last three points doesn't vary as shown in figure 22 (c). It gives almost the same values towards the end.

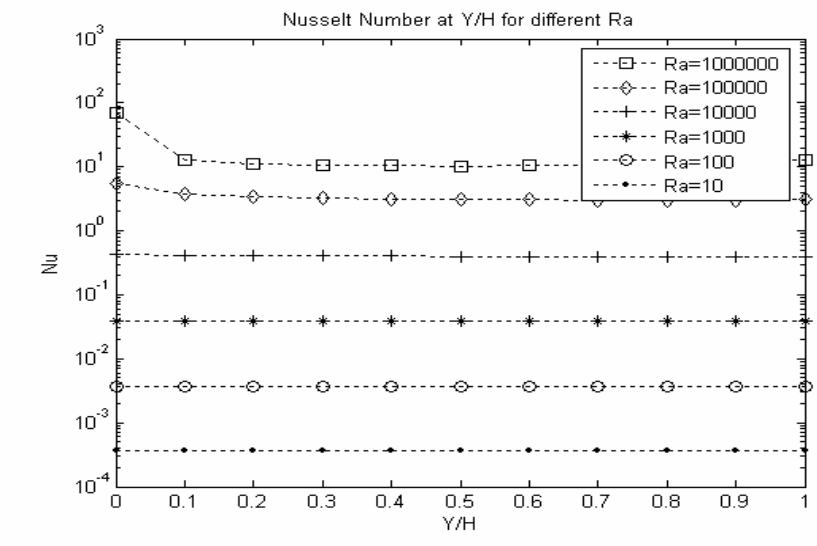

Figure 21: Local Nusselt number for different Rayleigh number

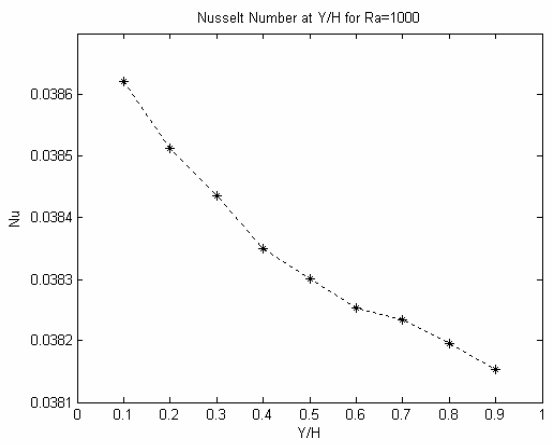

(a) Ra = 10^3

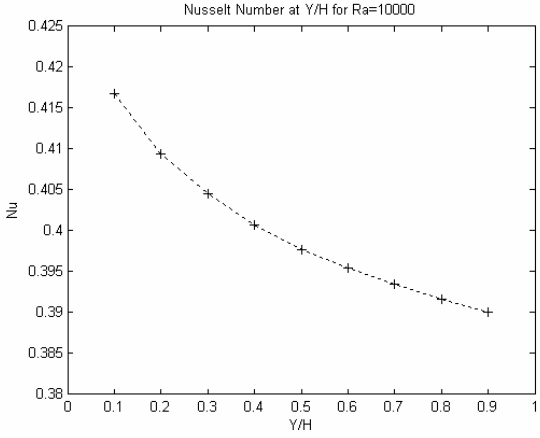

(b) Ra = 10^4

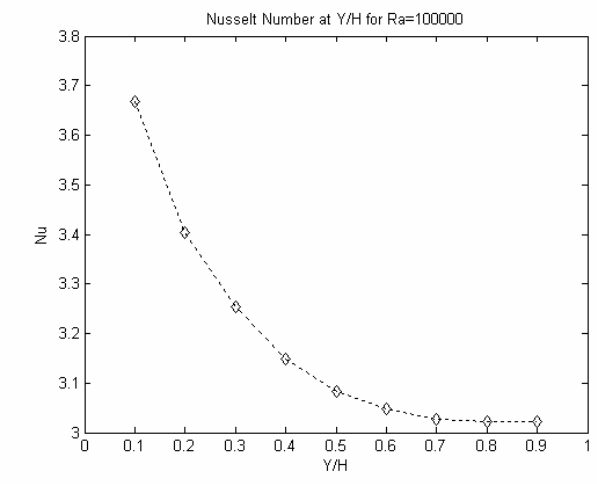

(c) Ra = 10^5

Figure 22: Local Nusselt number versus Y/H

4.1.5 Validation of the three-dimensional model with the two-dimensional results

Figure 8 shows the computational domain used for the three-dimensional smooth planar model. Special attention is given to mesh the three dimensional model to have the same resolution in the two directions as of the two-dimensional model. The velocity gradients along the Z-direction in smooth planar case are considered as negligible. As a result, the three-dimensional model should give the same results as the two-dimensional model. This comparison is done to cross check the computational accuracy since the result is already known. Moreover all other geometries are three dimensional models and so it is good to validate the three dimensional smooth planar results with the validated two dimensional results.

Figure 23 shows a plot of the Reynolds number versus the Rayleigh number for both three-dimensional and two-dimensional cases. It exhibits the same values for both the cases which validates the three dimensional model. Figure 24 shows a plot for the average Nusselt number versus the Rayleigh number for the three-dimensional and the two-dimensional cases. It shows a slight under-prediction for the highest Rayleigh numbers which can be considered as negligible. But the entire data is matching very well with the two-dimensional case.

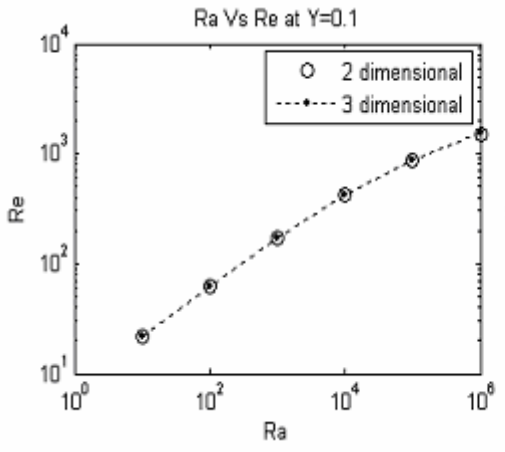

Figure 23: Re versus Ra for H= 200 mm

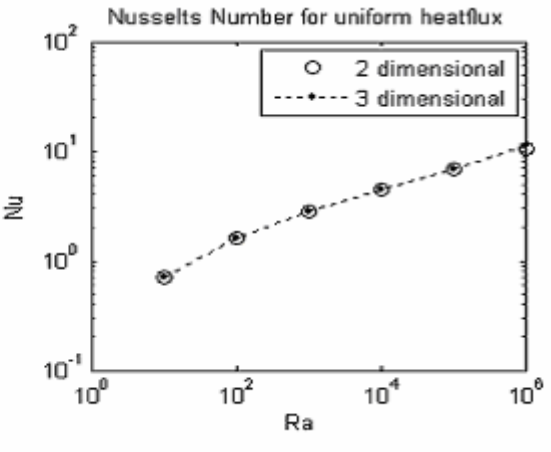

Figure 24: Nu versus Ra for H= 200 mm

4.1.6 Temperature distribution over the plates

Figure 25 shows the distribution of temperature over the smooth planar plate for Ra $=10^5$. The temperature gradients can be observed only along the Y-direction. Near the inlet, steep temperature gradients occur and the temperature increases as it moves away from the inlet. Higher heat transfer is near to the inlet while it decreases as it moves away from it.

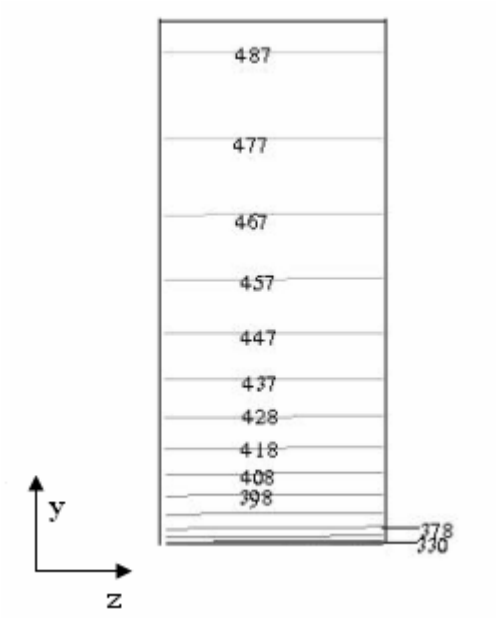

Figure 25: Temperature distribution of smooth planar

4.2 Smooth Folded

In this section the smooth folded case shown in figures 3 and 4 is compared with the smooth planar results. The range of Rayleigh numbers considered in the investigation of the smooth folded case slightly varies from the other cases (see section (3.3))

4.2.1 Average Nusselt number versus Rayleigh number

Figure 26 compares the plot for average Nusselt number versus Rayleigh number for the smooth planar and the smooth folded cases.

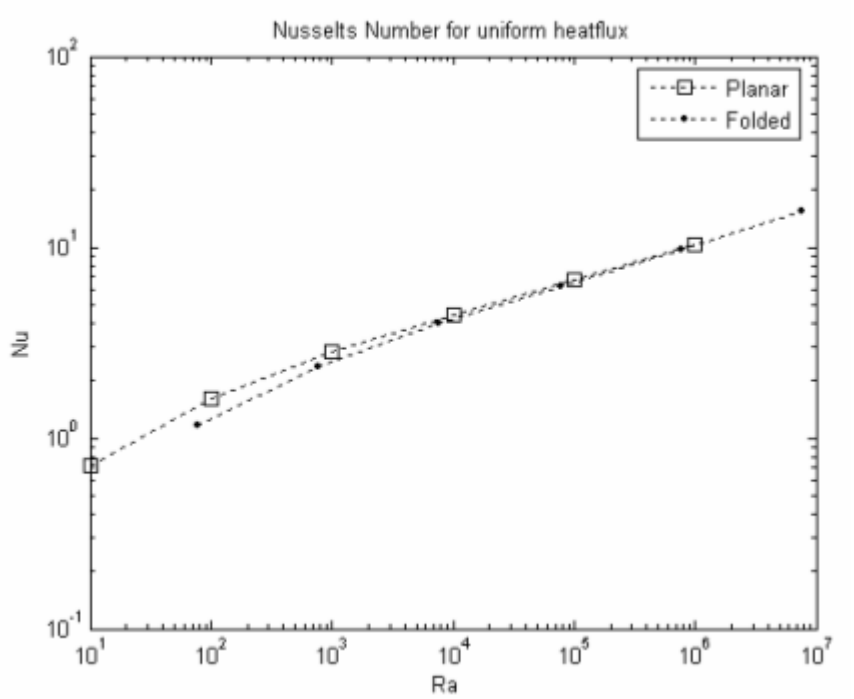

Figure 26: Ra versus average Nusselt number for the smooth planar and the smooth folded cases

The average Nusselt number of the smooth planar case is slightly higher than for the smooth folded case for low Rayleigh numbers. As the Rayleigh number increases the smooth planar Nusselt number becomes closer to that of the smooth folded case and when it reaches 10^{4}, the average Nusselt number for both the cases coincides and they continue to be the same for higher Rayleigh numbers.

There is however no significant difference between the two cases in the average Nusselt number versus Rayleigh number plot in the investigated Rayleigh number range.

4.2.2 Local Nusselt number versus Z

Figure 27 shows a plot of the local Nusselt number versus 'Z' at Y = 0.1 m for different Rayleigh numbers. The variations in local Nusselt number values are due to the folded geometry.

Figure 28 shows the behavior of the local Nusselt number at Y = 0.02 m, 0.1 m and 0 .2 m for Ra $=10^3$. At Ra = 10^3 , the local Nusselt number has a high value near the inlet and moving away from the inlet it decreases its value and it gives a minimum value at the outlet.

Figure 29 shows the plot of the local Nusselt number versus Z for Ra 10^3 to 10^5 at mid height. In figure 29 (a), for Ra $=10^3$ the local Nusselt number along the wall shows the same nature of the wall geometry while as the Ra number increases, the Nusselt number takes a curve as shown in figure 29 (b) and (c) which are corresponding to Rayleigh numbers 10^4 and 10^5 .

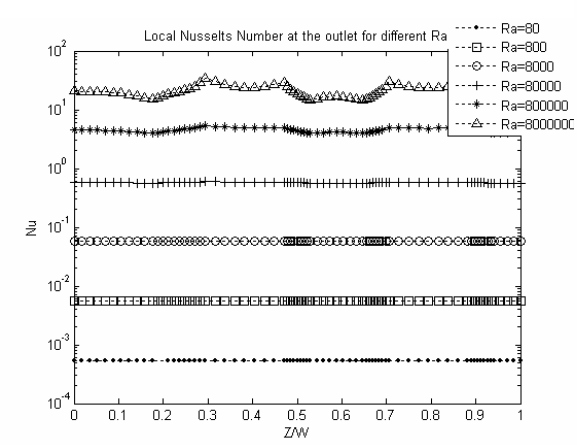

F igure 27: Local Nusselt number versus Z

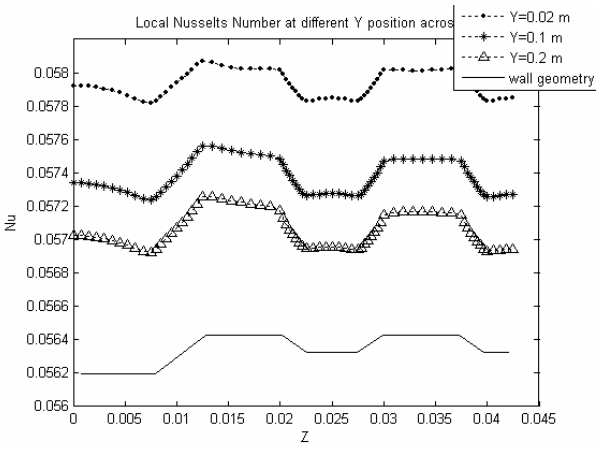

Figure 28: Local Nusselt Number versus Z at different downstream locations for Ra $=10^3$ .The wall geometry is shown as a reference

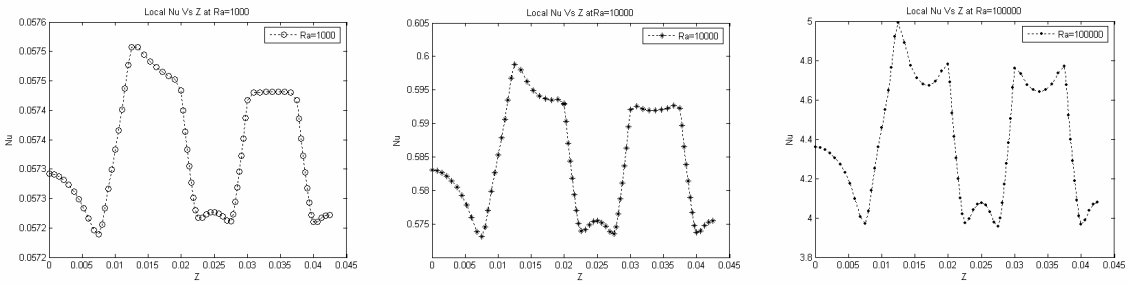

(a) *(b)* *(c)*

Figure 29: Local Nusselt number versus Z for different Ra at Y = 0.1 m

4.2.3 Reynolds number versus Rayleigh number

Figure 30 compares the Rayleigh number versus the Reynolds number for the smooth planar and the smooth folded cases. Here, the Reynolds number predicted for the smooth folded case is lower compared to the prediction of Reynolds number for smooth planar case in the range of Rayleigh numbers investigated. Increasing the H/S would result in increasing the Reynolds number for a particular Rayleigh number for the buoyancy driven flows between vertical plates is shown by Olsson C.-O. (2004). Hence in this particular investigation H/S is 10 for the smooth planar case while for the smooth folded case it is 6.667, which reflects the reason of the decrease in Reynolds number for the smooth folded case as compared with the smooth planar case in the figure 30.

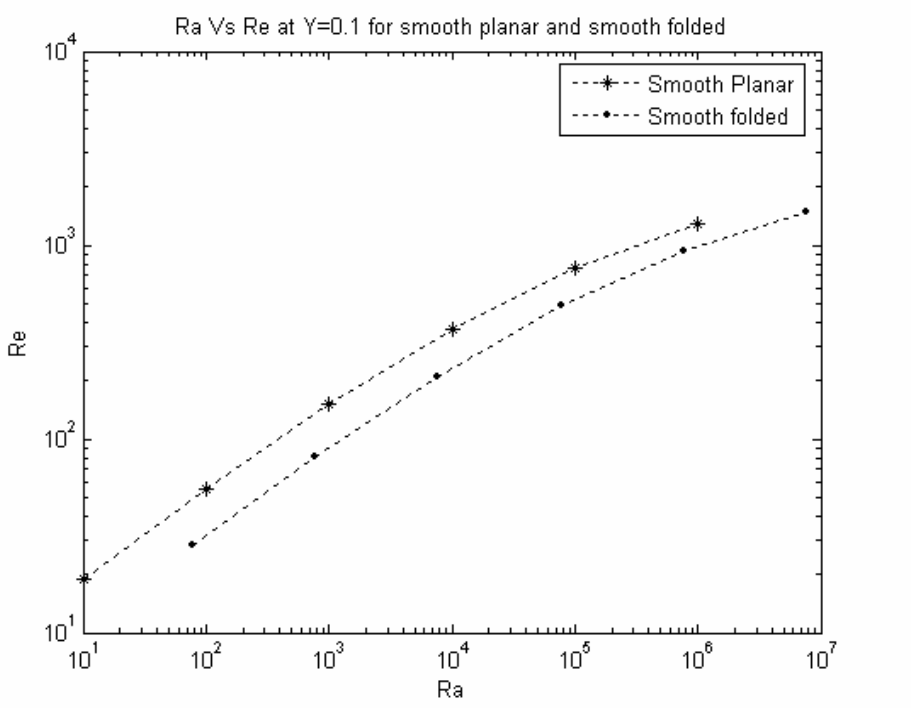

Figure 30: Rayleigh number versus Reynolds number for the smooth planar and smooth folded cases

4.2.4 Temperature distribution over the plates

Figure 31 shows the temperature distribution over the smooth folded plate for Ra $=10^5$. It is seen that, the region of the smooth folded plate which projects outwards the channel gives low Nusselt number and hence the high temperature distribution on those regions is visible. The low heat transfer on this region is compensated by the region of the smooth folded plate that is projected into the channel that gives low temperature distribution and high heat transfer. The high and low Nusselt numbers on the different regions of the smooth folded plate give rise to an average Nusselt number very close to the smooth planar case as shown in section (4.2.1).

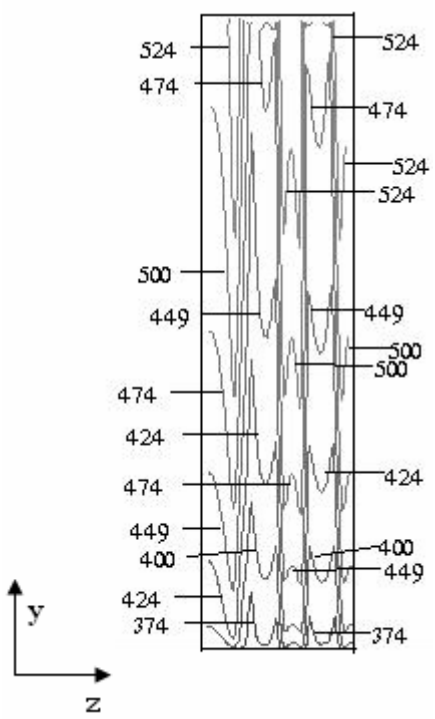

Figure 31: Temperature distribution for smooth folded geometry

4.3 Multiple V-shaped Rib Geometry

The rib geometry creates a secondary flow which exchange heat and momentum between the wall regions and core regions. The roughness on the plate increases the heat transfer coefficient, but it also increases the pressure drop. Choosing parameters like angle of attack, rib angle and pitch to height ratios are important in the optimization of the heat transfer in this particular geometry. It should be chosen to have a minimum increase in pressure drop and a maximum increase in heat transfer. For this investigation, parameters are chosen based on the investigations done by Olsson & Sunden (1998) and Olsson (1999). The results are compared with results from the other geometries.

The cases investigated for the multiple V-shaped rib geometry is shown in table 6

4.3.1 Average Nusselt number versus Rayleigh number

Figure 32 shows the plot of the average Nusselt number versus the Rayleigh number for the smooth planar and the multiple V-shaped rib geometry for H = 200 mm. For the lowest Rayleigh numbers the average Nusselt number on the V-rib plates are lower than the smooth planar cases. But after a critical value (Ra = 1490), the V-rib geometry will have higher heat transfer than the smooth planar case.

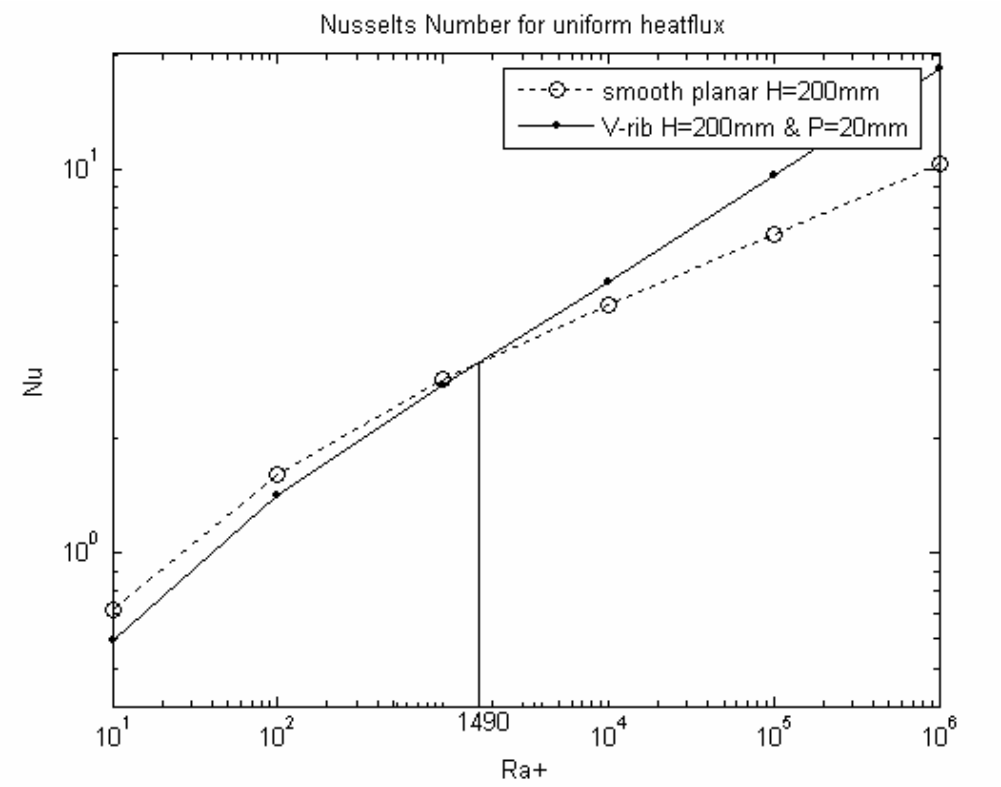

Figure 32: Nu versus Ra for smooth planar and V-rib for H=200mm

With the increase in channel height, the mass flow rate inside the channel is increased. As a result, the Reynolds number in the channel will increase by increasing the heat transfer due to natural convection. Figure 33 shows a plot of the average Nusselt number versus Rayleigh number for the smooth planar and the V-rib cases for H = 400 mm.

It can be seen from figure 33 that a decrease in the number of ribs would increase the heat transfer rate to some extent. But the smooth planar case, which can be considered as the rib geometry with infinite pitch length, has the lowest Nusselt number. As a result it is obvious that decreasing the pitch after a particular limit would tend to decrease the Nusselt number instead of increasing it. The critical Rayleigh number at which the Nusselt number for the V-rib geometry crosses the smooth planar case is decreased further with the increase of height. For 20 mm pitch it gives a higher Nusselt number from Ra = 740 and for 40 mm pitch critical Ra is further decreased to 490 as shown in figure 34. However when the rib height is increased to 4 mm from 2 mm, the critical Ra is also increased to 1200.

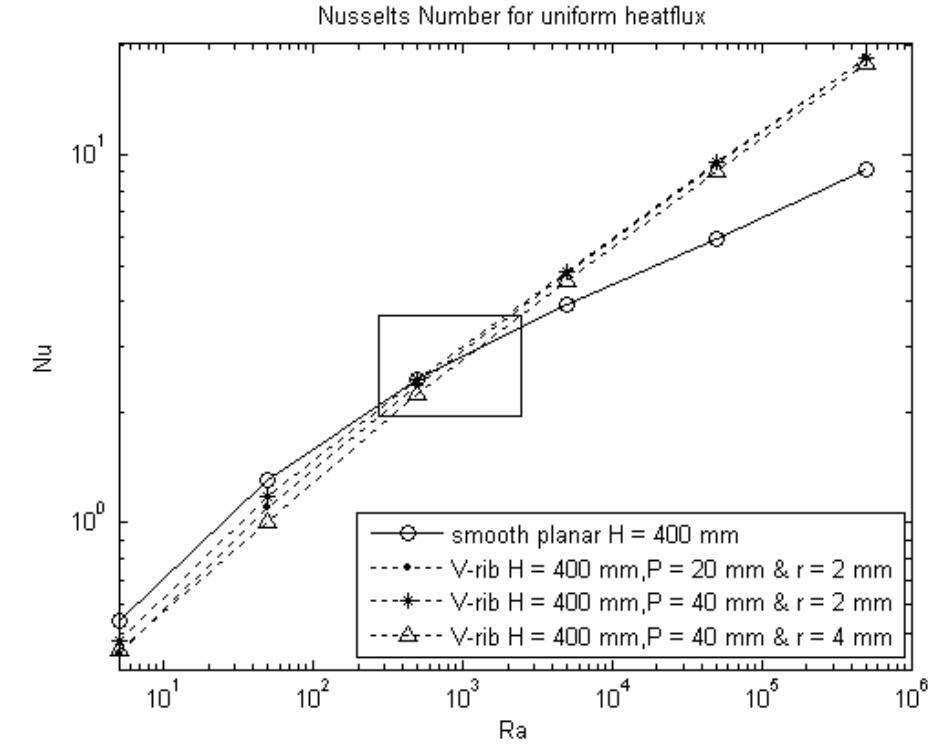

Figure 33: Average Nusselt number versus Rayleigh number

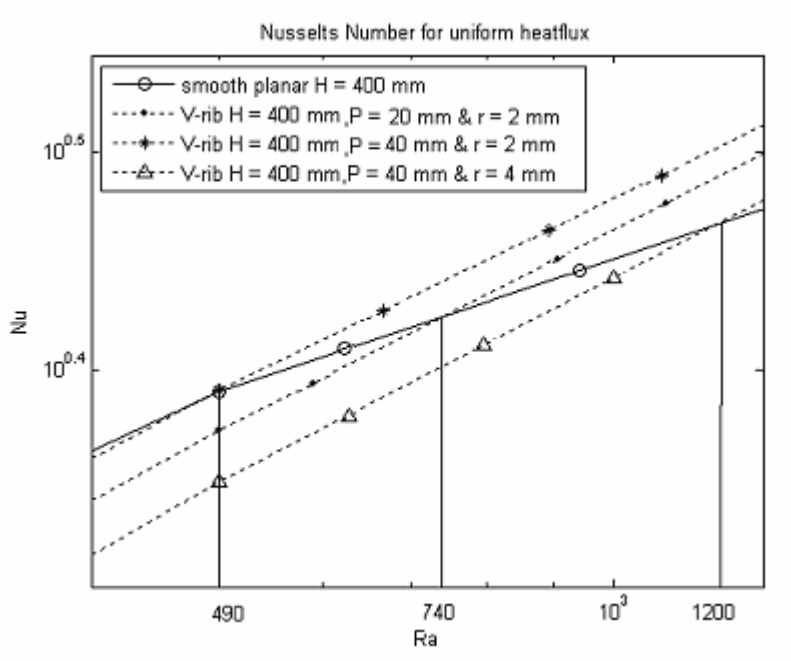

Figure 34: portion inside the box in figure 33

Figure 35 shows ratio of the Nusselt number for the rib geometry and the smooth planar case versus Ra plot for H = 200 mm and H = 400 mm for both the pitch lengths considered. In the region below the straight dotted line (Nu-rib/Nu-smooth = 1), all the geometries give Nusselt numbers lower than the smooth planar case. At low Rayleigh number, ribs on the geometry would tend to resist the flow by reducing the Nusselt number. But increasing the height and pitch tend to improve the heat transfer of the V-rib geometry. However, when the rib height is increased to 4 mm from 2 mm it gives a lower Nusselt number.

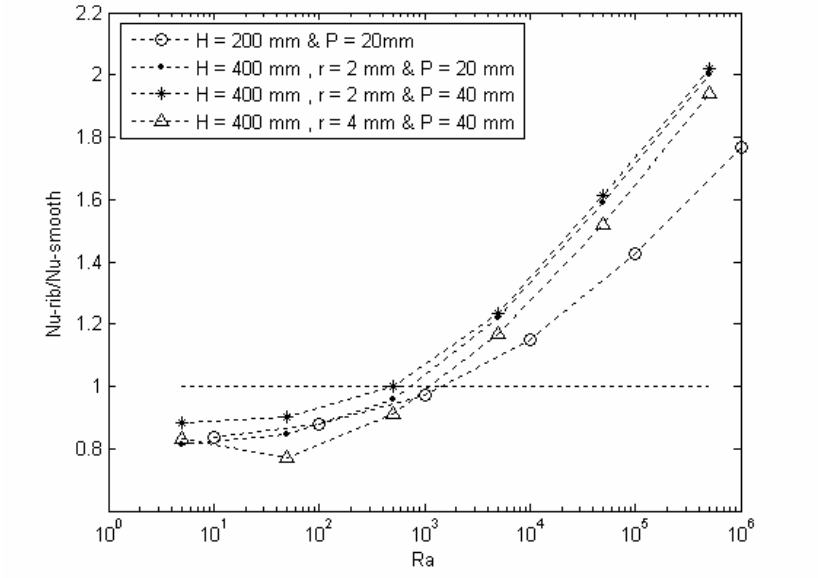

Figure 35: Nu-rib/Nu-smooth planar versus Ra

Figure 36 shows the Nu-rib/ Nu-smooth planar versus Re plot for H = 200 mm and H = 400 mm for P = 20 mm and P = 40 mm and for r = 2 mm and r = 4 mm. V-rib geometry gives almost the same Nusselt numbers for the same value of Reynolds numbers for the highest Rayleigh numbers for different pitch lengths, while the smooth planar geometry gives higher Nusselt numbers for lower Reynolds numbers. Figure 35 and 36 shows that the variation of Nusselt number for the V-rib geometry with respect to the corresponding smooth planar case for different parameters of the V-rib doesn't depend much on the Reynolds number.

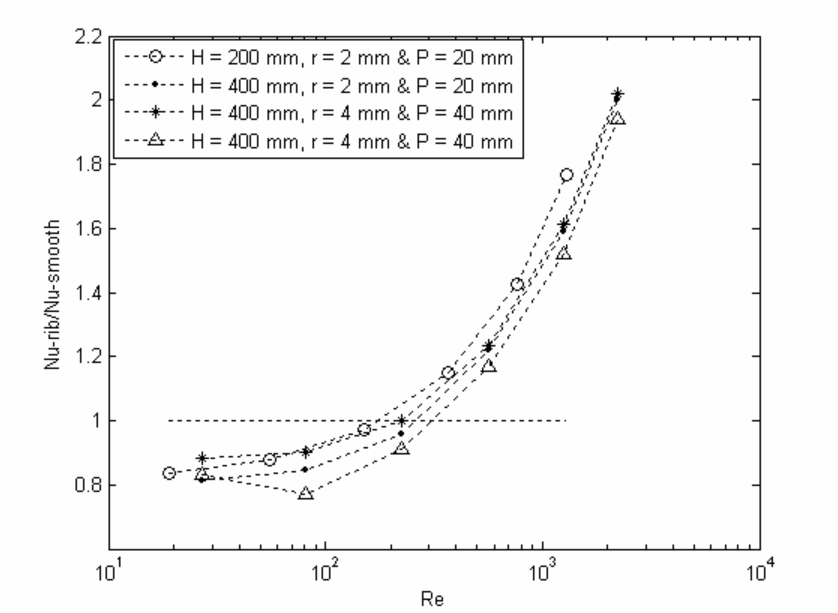

Figure 36: Nu-rib/Nu-smooth planar versus Re

4.3.2 Local Nusselt number versus Z

Figure 37 shows a plot of the local Nusselt number versus Z at Y = 0.1 m for P = .02 m and H = 0.2 m. With an increase in Rayleigh number, the local Nusselt number across the plate also increases since the heat flux given on the plates are higher for higher Rayleigh numbers.

Figure 38 (a) shows the plot of the local Nusselt number versus Z at different downstream locations for the V-rib pointing downstream while Figure 38 (b) shows the plot for the V-rib pointing upstream. Both gives high Nusselt number in the inlet and decreases as it goes downstream. A higher heat transfer occurs near the inlet. Due to the ribs throughout the geometry, secondary flow is generated and it gives a higher heat transfer coefficient where the secondary flow tends to transport more heat into the flow.

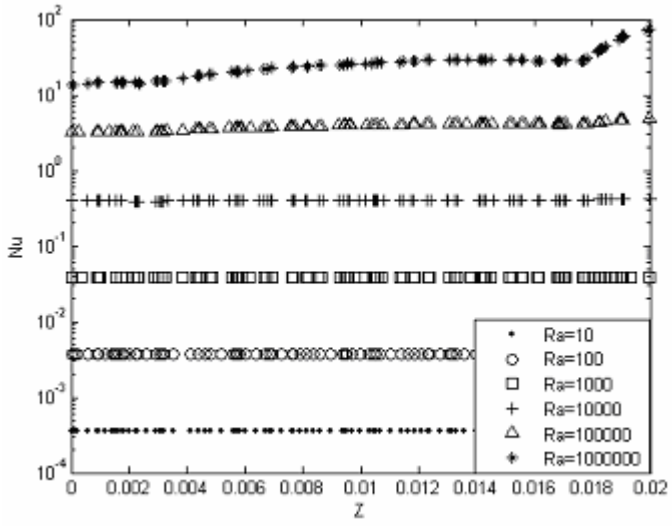

Figure 37: Local Nusselt number versus Z at y= 0.1 m at different Ra

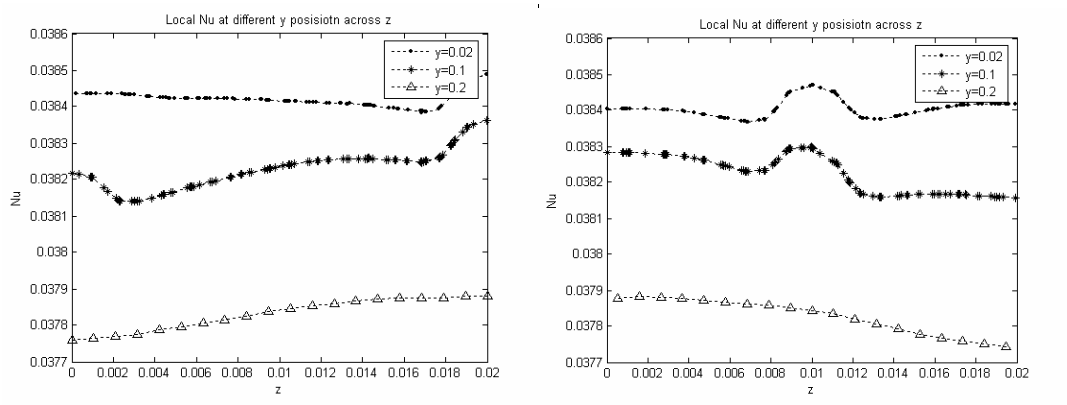

(a) *(b)*

Figure 38: Local Nusselt Number Versus Z at different downstream locations for Ra $= 10^3$

4.3.3 Reynolds number versus Rayleigh number

Figure 39 shows the plot of the Reynolds number versus the Rayleigh number with different parameters for the multiple V-rib geometry and for the smooth planar case. It is seen that the Reynolds number increases with increasing Rayleigh number. Increasing the duct height corresponds to increasing the Reynolds number. Almost for all Rayleigh numbers, the smooth planar channel gives a higher Reynolds number with respect to the V-rib geometry. When the rib height is increased from 2 mm to 4 mm, it resists the flow in turn reducing the Reynolds number as compared to the other V-rib cases.

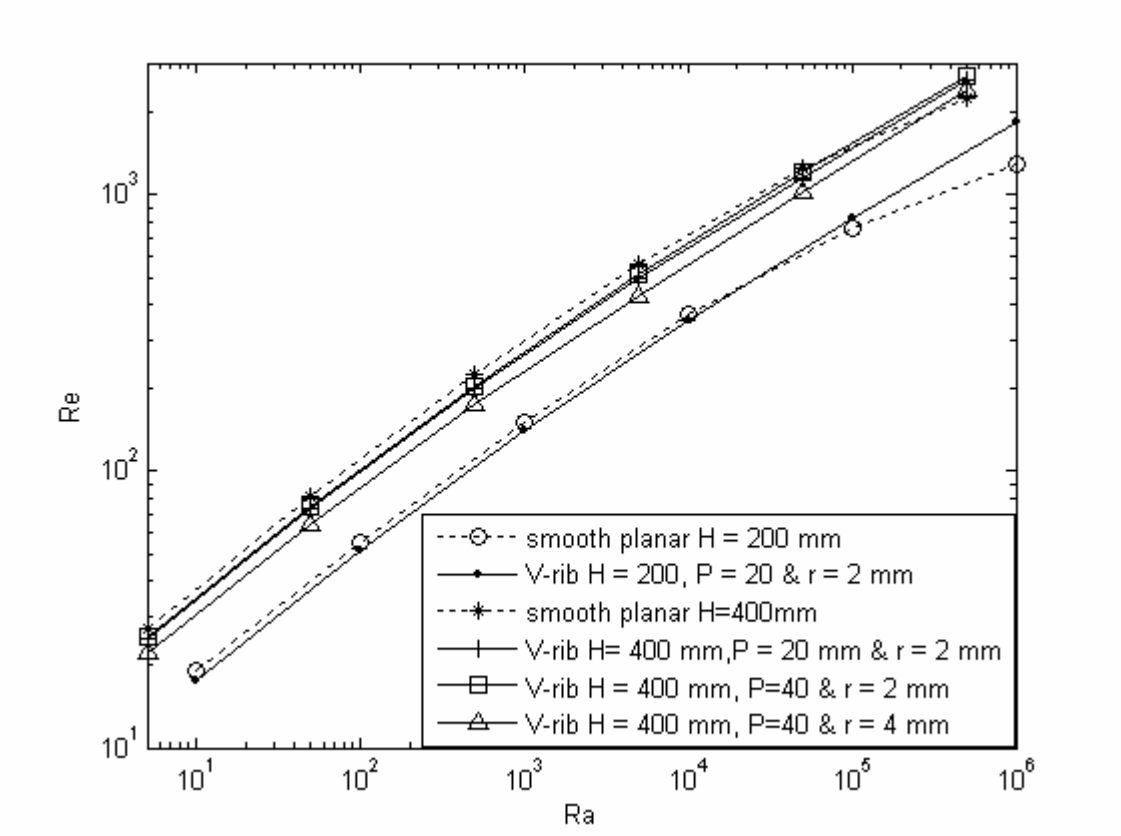

Figure 39: Reynolds Number versus Rayleigh Number

4.3.4 Temperature distribution over the plates

Figure 40 (a) shows the positions of V-ribs with respect to the flow while figure 40 (b) shows the temperature distribution between the two ribs. For uniform heat flux boundary condition, the region of the plate with high temperature has less heat transfer and the region with lower temperature has the high heat transfer. The rib geometry creates secondary flow which exchange heat and momentum between the wall regions and core regions. The edge with higher temperature will have the vortices directed away from it. As a result, less heat transfer occurs in that edge. While the other edge will have the vortices impinging on it that cause to extract more heat from the edges resulting in high heat transfer. Temperature distribution in this edge gives lower temperature.

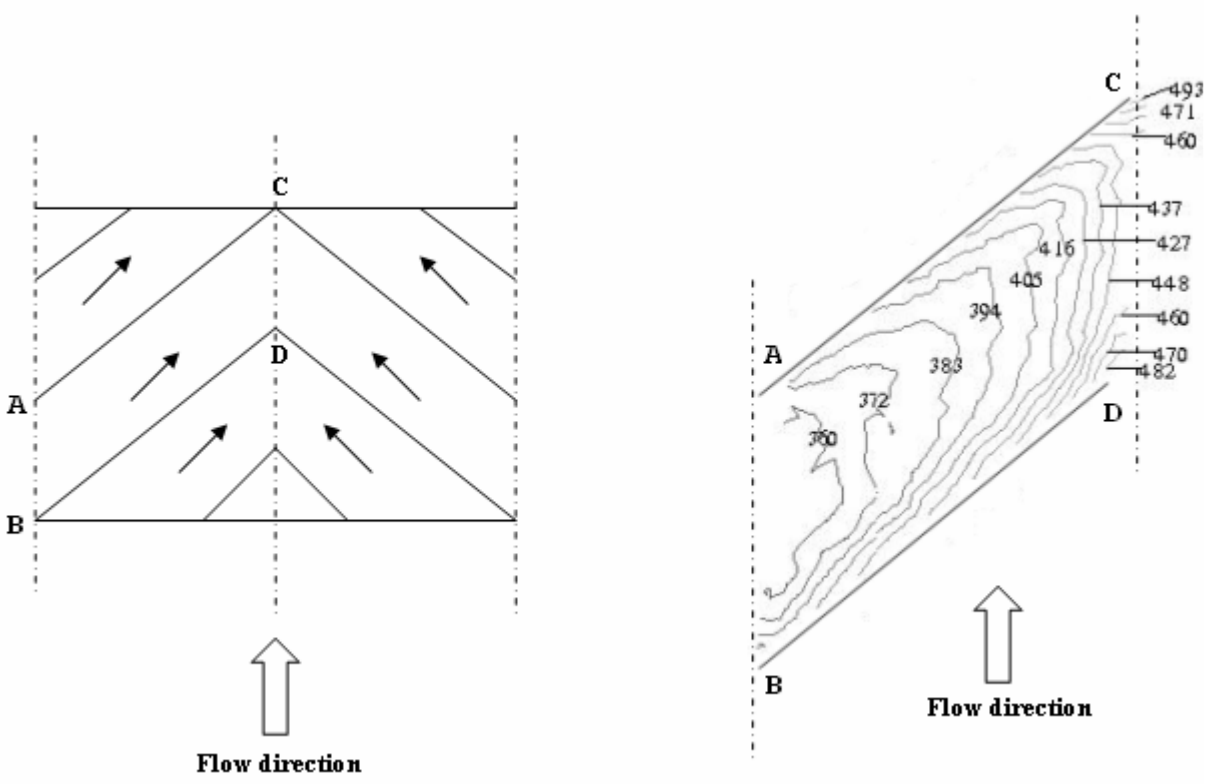

(a) Position of V-ribs with respect to flow direction *(b) Temperature distribution between two ribs*

Figure 40: Temperature distribution for the V-rib geometry

4.3.5 Velocity vectors at the mid-plane of the V – rib geometry

Figure 41 shows the velocity vectors of the V-rib geometry at Y = 0.2 m for Ra =10^5 . Here the velocity vectors clearly show the presence of secondary flow along the X and Z-direction while the air flow is in Y-direction. Ribs on the plate induces a secondary flow as shown in figure 41 which in turn mixes the flow well and enhances the heat transfer in a duct .

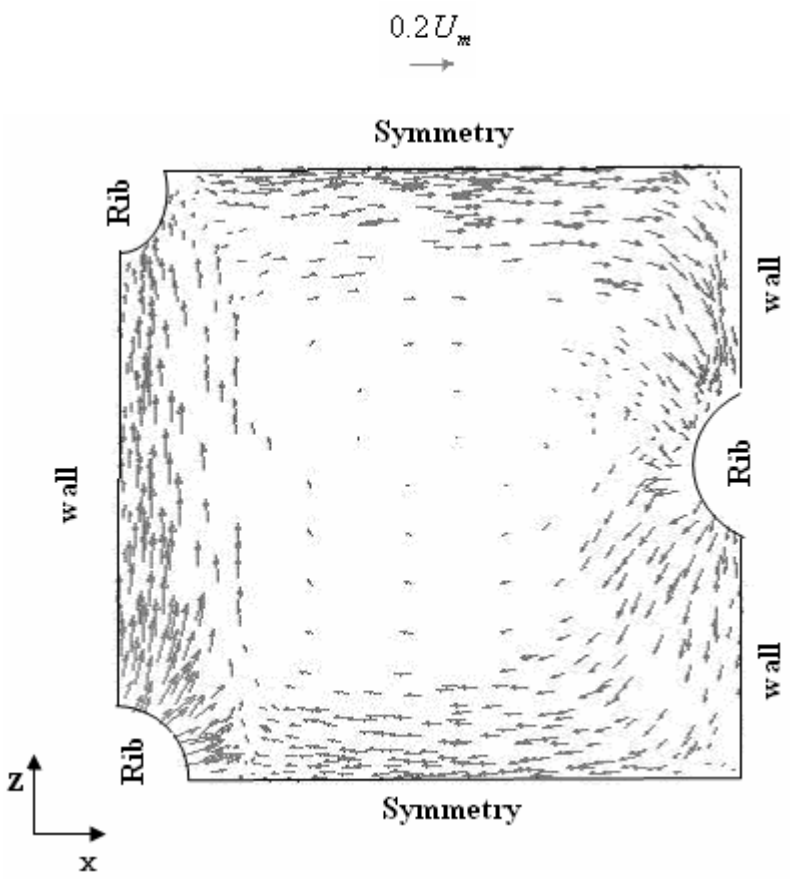

Figure 41: Velocity vectors at mid- plane of the V-rib geometry of H = 400 mm at Ra = 10^5

4 CONCLUSION

Numerical results have been presented for the buoyancy-driven flow of air between parallel plates with uniform heat flux for three different geometries. The physics of the problem and the heat transfer characteristics have been discussed for all the three geometries at a wide range of Rayleigh numbers.

The flow and the heat transfer characteristics of the smooth planar case is analyzed and validated with the available correlations. The Nusselt number on the smooth folded plate doesn't vary much with respect to the smooth planar plate.

Ribs on the wall create secondary flow which exchange heat and momentum between the wall regions and core regions. Wall with ribs on it gives higher Nusselt number compared to the smooth planar case for all range of Rayleigh numbers except for the lowest Rayleigh numbers. Different parameters like pitch, height and rib height are varied and the effect of it on the heat transfer characteristics is evaluated. It is noticed that decreasing the number of ribs until a certain limit would result in an increase in the Nusselt number and doubling the height also results in an increase in heat transfer coefficient. However, increasing the rib height tends to decrease the heat transfer coefficient compared to the other V-rib cases of the same height.

5 REFERENCES

Bar-Cohen, A., and Roshenow, W.M., 1984, "Thermally optimum spacing of vertical, natural convection cooled parallel plates", *ASME J. HEAT TRANSFER*, Vol. 106, pp. 116-213.

Bodoia, J.R., and Osterle, J.F., 1962, "The development of free convection between heated vertical Plates", *ASME J. HEAT TRANSFER*, Vol. 84, pp. 40-44.

Chang, T., S., and Lin, T., F., 1989, "Transient buoyancy-induced flow through a heated, vertical channel of finite height", *Numerical Heat transfer,* Vol. 16, pp. 15-35.

Elenbaas, W., 1942, "Heat Dissipation of Parallel Plates by Free Convection", *Physica*, Vol. 9, No. 1, pp. 1-28.

Gray, D.D., Giorgini, A., 1975, "The validity of the boussinesq approximation for liquids and gases", *Int. J. Heat Mass Transfer,* Vol. 19, pp. 545-551.

Kettleborough, C. F., 1972, "Transient laminar free convection between heated vertical plates including entrance effects", *Int. J. Heat Mass Transfer,* Vol. 5, pp. 883-896.

Morrone, B., Campo, A., and Manca, O., 1997, "Optimum plate separation in vertical parallel-plate channels for natural convective flows: Incorporation of large spaces at the channel extremes", *Int. J. Heat Mass Transfer*, Vol. 40, pp. 993-1000.

Nakamura, H., Yutaka, A., and Naitou, T., 1982, "Heat transfer by free convection between two parallel flat plates", *Numerical Heat transfer,* Vol. 5, pp. 95-106.

Olsson, C.O., Sunden, B., 1997a, "Fluid flow and heat transfer in rib roughened tubes", *Experimental Heat transfer, Fluid Mechanics and Thermodynamics 1997*(Eds. Goit, M., Mayinger, F. and Celata, G.P), Vol. 3, pp. 1655-1662, Edizioni ES, Pisa.

Olsson, C.O., Sunden, B., 1997b, "Experimental study of flow and heat transfer in rib-roughened channels", *Exp. Thermal Fluid Sci*., Vol. 16, pp. 349-365.

Olsson, C.O., Sunden, B., 1998, "Thermal and hydraulic performance of a rectangular duct with multiple V-shaped ribs", *ASME J. HEAT TRANSFER,* Vol.120, pp.1072-1077.

Olsson, C.O., 1999, "Flow and heat transfer in passages with multiple V-ribbed walls", *Progress in engineering heat transfer,* pp. 561-568.

Olsson, C.O., 2004, "Prediction of Nusselt number and flow rate of buoyancy vertical plates", *ASME J. HEAT TRANSFER*, Vol.126, pp. 97-103.

Ramanathan, S. and Kumar, R., 1991, "Correlations for natural convection between heated vertical plates", *ASME J. HEAT TRANSFER,* Vol.113, pp. 97-105.

Roshenow, W. M, Hartnett, J.P, and Cho, Y.I, eds., 1998, *Handbook of Heat Transfer,* McGraw-Hill, New York.

Shyy, W., Gingrich, W. K., and Gebhart, B., 1992, "Adaptive grid solution for buoyancy-induced flow in vertical slots", *Numerical Heat Transfer*, Part A, 22, pp. 51-70.